



HAL
open science

A multi-scale approach to investigate the non linear subsurface behavior and strain localization of X38CrMoV5-1 martensitic tool steel: experiment and numerical analysis

Ahmed Zouaghi, Vincent Velay, Adriana Soveja, Thomas Pottier, Mohammed Cheikh, Farhad Rezai-Aria

► To cite this version:

Ahmed Zouaghi, Vincent Velay, Adriana Soveja, Thomas Pottier, Mohammed Cheikh, et al.. A multi-scale approach to investigate the non linear subsurface behavior and strain localization of X38CrMoV5-1 martensitic tool steel: experiment and numerical analysis. *International Journal of Plasticity*, 2016, 87, pp.130-153. 10.1016/j.ijplas.2016.09.007 . hal-01398857

HAL Id: hal-01398857

<https://hal.science/hal-01398857>

Submitted on 17 Nov 2016

HAL is a multi-disciplinary open access archive for the deposit and dissemination of scientific research documents, whether they are published or not. The documents may come from teaching and research institutions in France or abroad, or from public or private research centers.

L'archive ouverte pluridisciplinaire **HAL**, est destinée au dépôt et à la diffusion de documents scientifiques de niveau recherche, publiés ou non, émanant des établissements d'enseignement et de recherche français ou étrangers, des laboratoires publics ou privés.

A multi-scale approach to investigate the non linear subsurface behavior and strain localization of X38CrMoV5-1 martensitic tool steel: experiment and numerical analysis

A. Zouaghi^{a,b}, V. Velay^{a,*}, A. Soveja^a, T. Pottier^a, M. Cheikh^a, F. Rézaï-Aria^a

^a*Université de Toulouse; CNRS, Mines Albi, INSA, UPS, ISAE, ICA (Institut Clément Ader), Campus Jarlard, 81013 Albi Cedex 09, France*

^b*ArcelorMittal, Global R&D Maizières Research, BP 30320, 57283 Maizières-lès-Metz Cedex, France*

Abstract

The cyclic mechanical behavior, the wear and fatigue resistances and damage developments of working surface of tool steels are dependent on microstructural features. A multi-scale approach combining experimental testing, numerical treatments and simulations is developed to model the surface behavior of X38CrMoV5-1 martensitic tool steels. The multi-scale modeling is coupled with finite element calculations. The elasto-viscoplastic constitutive equations used are based on crystal plasticity model of Méric-Cailletaud and are implemented on the finite element code ABAQUS under a small strain assumption. Through an appropriate laboratory testing, the microstructure features comparable to the surface of industrial tools or pin/disc in tribology experiments are reproduced by considering plate specimens. Monotonic tensile testing is coupled with in-situ Digital Image Correlation technique (DIC) to determine the surface strain fields. The measured local nonlinear mechanical strain fields are analyzed. The strain localization is related to stereological artifacts. The numerical treatments allow reproducing, qualitatively, the strain localization patterns at the surface observed during tensile testing. The influence of the various stereological parameters such as the morphology of martensitic laths, the crystallographic orientations, the internal hardening state of the surface profiles and their evolutions on the local strain fields are addressed. By such approach, it is possible to get a better insight of some elementary mechanisms acting on tools and/or pin/disc surfaces regarding both tensile and cyclic behavior.

Keywords: A.microstructures, B.crystal plasticity, B.cyclic loading, C.mechanical testing, surface behavior

1. Introduction

During forming operations such as forging, rolling, stamping ..., and more specifically at high temperatures, the tool surfaces experience thermal and mechanical

*Corresponding author

Email address: vincent.velay@mines-albi.fr (V. Velay)

4 cyclic loadings under transient conditions. Fatigue and wear are the two main dam-
5 age mechanisms of tool surfaces. Depending on tool geometry and local thermo-
6 mechanical loading, fatigue or wear may become the leading damage mechanism.
7 At the stress raiser regions (e.g. tool radii, holes, ...) uni-axial cracking is generally
8 dominant while the local loading is at least bi-axial state on plane surface and the
9 interconnected cracks pattern called *heat checking*, is mostly observed in these re-
10 gions. The tool surface is subjected to local plastic yielding especially at singularity
11 locations (e.g. corners and stress raisers). These damage mechanisms can also act
12 simultaneously and in coupling with environment such as oxidation or corrosion (in
13 die casting). The prediction of the tool life is of primary concern for tool design-
14 ing and damage monitoring. The interruptions in production because of premature
15 tools damaging are very time consuming in term of reparation and are highly cost
16 effective. Therefore, the lifetime prediction is a major issue for optimizing the tool
17 design. These approaches require relevant thermo-mechanical constitutive models.
18 However, such models are generally addressed using a RVE (Representative Volume
19 Element) features and consider the material as *isotropic* in behavior. Neverthe-
20 less, almost all tool surfaces present very early *microstructure* texturing at different
21 scales : macroscopic, mesoscopic and microscopic. Such microstructural evidences
22 show that constitutive laws must take into account the anisotropic behavior near
23 the working surfaces. It should be emphasized that such changes in extreme surface
24 of tools are very common features that cover many surfaces of bodies in relative
25 movements and presenting certain shear ductility. In fact, in contact surface, a few
26 grains bear the whole load. As the elasto-plastic behavior of a grain is *physically*
27 dominated by the nature of the crystal lattice and its actual orientation regard-
28 ing the local main loading axis, it is senseless to consider an *isotropic* constitutive
29 law. By definition the surfaces are singular for chemical reactions, mechanical be-
30 haviors and damage developments. Therefore, a special attention must be paid to
31 the *anisotropic nature* of the surface when it experiences shearing. Thus, *crystal*
32 *plasticity models* with *multi-scale* approaches have to be addressed. They can im-
33 prove the description of the local behavior at tool surface vicinity ($\approx 100 \mu m$), while
34 classical macroscopic approaches are worthless for such matter. They include a lo-
35 cal behavior model able to take into account both representative external loading
36 and the slip system interactions of the martensitic BCC (Body-Centered Cubic) mi-
37 crostructure [1] as is the case for hot work tool steels. Some elementary physical
38 mechanisms are introduced in these approaches for describing the cyclic plasticity
39 [2–4] through a non linear kinematic variable [5, 6]. These models can be improved
40 by taking into account the influence of the total dislocation densities with strain
41 for each slip system [7] and by introducing an isotropic hardening variable [8, 9].
42 Different yield surfaces can be associated to the physical phenomena like the screw
43 and edge dislocation effects [10, 11]. However, the parameters identification of such
44 models is not trivial. Phenomenological approaches are based on thermodynamics
45 of the irreversible process. The constitutive equations are very similar to the formu-
46 lations addressed in the physical approaches. Again, the shear strain rate is related
47 to the resolved shear stress [12]. Many investigations consider an isotropic harden-
48 ing variable to describe different slip systems interaction by introducing latent and
49 self hardening mechanisms [13–16]. The kinematic hardening can be included by

50 using the Armstrong-Frederick or Chaboche equations [17]. The model parameters
51 can then be identified using either a mean field or a full field approach. Berveiller
52 and Zaoui [18] propose a scale transition rule to describe the monotonic behavior
53 of spherical particules. Later, Pilvin and Cailletaud propose an extension of the
54 Berveiller-Zaoui model, the β -model [19], that accounts for cyclic loadings. The
55 mean field approaches are relevant for identifying the material parameters at a local
56 scale. However, they strongly depend on the linearisation methods used at the local
57 and global scales. For this purpose, full fields approaches are more accurate and
58 better describe the behavior of a given RVE. They explicitly take into account the
59 internal structure of the material (morphology, crystallography, nature ...) [3, 4] and
60 provide a spatial localization of mechanical fields [20–26]. Obviously, the resulting
61 calculations are more reliable than those induced by a mean field model though
62 being more expensive. One of the method employed in scale transition rule is FE
63 (Finite Element) method. It consists in solving a macroscopic boundary problem in
64 coupling with RVE which considers the actual microstructure features of the mate-
65 rial. In such approaches, the constitutive equations are solved at each integration
66 point of the FE mesh. The strain fields obtained at a local scale can be compared to
67 local experimental measurements by Digital Image Correlation techniques [27–31].
68 In this frame, the FE analysis can be used to assess the reliability of the mean field
69 simulations [32].

70 In the present investigation, the Meric and Cailletaud model [33–35] is used for
71 predicting the surface behavior of hot forming tools (e.g. forging) and pin-on-disc
72 tests [36, 37]. It should be emphasized that the surface of hot forming tools ex-
73periences actually transient thermo-mechanical wear and fatigue solicitations. The
74 crystal plasticity models are adequate to take into account the crystallography fea-
75tures such as plastic anisotropy [38] and temperature dependence of physical and
76 mechanical properties in particular for BBC and tetragonal lattice structures like
77 martensitic material reported here [39]. Due to experimental difficulties for high
78 temperature strain field measurements, the model capability was first assessed at
79 room temperature. Nevertheless, the model is expressed for being easily applied
80 both at isothermal and transient thermomechanical conditions. The mean field ap-
81proach is performed for parameter identification sake. The scale transition rules,
82 Berveiller-Zaoui and β models are considered. The results are compared with those
83 obtained by a full field approach. This latter uses a FE calculation at the scale
84 of the RVE. In this case, the actual microstructure of tool steel is explicitly taken
85 into account. The constitutive equations are implemented on ABAQUS software.
86 The martensitic microstructure is modeled by using Voronoï tessellation and Neper
87 software [40]. A parametric analysis is undertaken to assess the effect of several
88 factors, namely: surface hardening, surface anisotropy, crystallographic orientation,
89 grain/lath morphology, on the local and global induced mechanical fields. All these
90 criteria can influence the surface properties and the material [4]. In some cases, a
91 geometrically realistic microstructure can have more important effects on the hetero-
92geneous deformation processes than a fine tuning of the constitutive model param-
93eters [41]. A recent investigation have shown that a multiscale framework with an
94 explicit representation of tempered martensitic microstructure accurately describes
95 the typical softening effects due to precipitate and lath coarsening [42]. In this study,

96 the local behavior model allows to take into account the laths shape and the slip
 97 systems interactions of the BCC martensitic microstructure. Two kinds of experi-
 98 ments are conducted. First, tests are performed on flat specimens to generate the
 99 typical surface observed on industrial tools. These specimens experience monotonic
 100 tensile loading. The surface roughening and its influence on the strain heterogeneity
 101 and grain localization is investigated since these interactions can have a significant
 102 effect on the mechanical behavior [43]. Multiscale modeling is a relevant approach
 103 to catch such kind of phenomena [44]. In this frame, DIC technique allows high
 104 resolution strain mapping [45] and therefore are relevant to compare the local mea-
 105 sured strain fields with the results provided by the FE simulation. The interplay
 106 between simulation results and experiment provided by full field measurements at
 107 a local scale is not trivial to perform especially when complex microstructures are
 108 considered [46]. Last, the multi-scale modeling is extended to describe the cyclic
 109 behavior and the results are analyzed regarding the previous factors investigated
 110 under monotonic conditions.

111 2. Experimental procedures

112 2.1. Material

113 The material investigated is a 5% chromium double tempered martensitic steel
 114 (X38CrMoV5-1, AISI H11). Its chemical composition is reported in table 1.

Table 1: Chemical composition wt.%

C	Cr	Mn	V	Ni	Mo	Si	Fe
0.4	5.05	0.49	0.47	0.2	1.25	0.92	Bal.

115 The heat treatments results in an initial hardness of 47 HRC with a tempered
 116 martensitic lath microstructure. In fact, the microstructure consists of ferrite and
 117 cementite in form of lath (Fig. 1). The lath morphology is quite heterogeneous
 118 with an average thickness less than $2 \mu m$. The laths are arranged by packets within
 119 the Prior Austenitic Grains (PAG) whose mean size is around $30 \mu m$. EBSD (Elec-
 120 tron BackScatter Diffraction) analysis have revealed that global crystallographic
 121 orientations of the grain is isotropic which confer to the steel an isotropic behavior.
 122 However, following early motion between tool and formed material (alt. between pin
 123 and disc), the grains are stretched along the sliding direction. By EBSD, the crystal-
 124 lographic orientation relationships of the martensitic laths (Body-Centered Cubic)
 125 and the PAG (Face-Centered Cubic) lattices are identified. Several approaches can
 126 be found to assess these orientation relationships [47, 48]. In the present study,
 127 the PAG wherein the martensitic lath blocks are stacked, is analyzed by using the
 128 crystallographic orientations. It is observed that the morphology of the martensitic
 129 laths are arranged in a quasi-parallel manner (see Fig. 2). The microstructure ex-
 130 hibits a high density of dislocations, which gives a good strength to the steel at room
 131 temperature. Many investigations have clearly shown that the steel is highly prone
 132 to cyclic softening [49–51]. In addition, The Low Cycle fatigue (LCF) experiments
 133 have shown a significant softening for the first hundred cycles following a linear *con-*
 134 *tinuous* softening until the rupture.

135

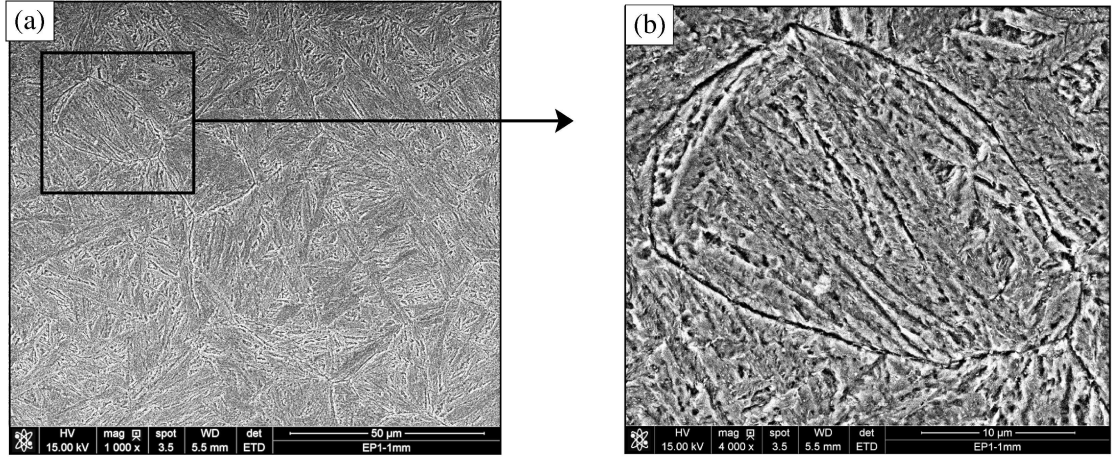


Figure 1: SEM observations of X38CrMoV5-1 steel: martensite lath microstructure (a) with prior austenitic grain (b).

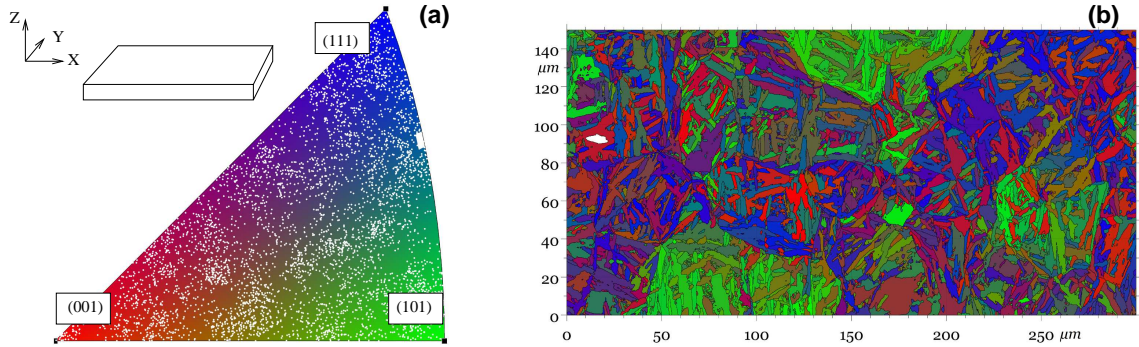


Figure 2: Inverse pole figure according X axis, white dots correspond to the orientation of each martensitic lath (a); Spatial distribution of the orientations (b).

136 2.2. Surface grain texturing

137 The forging tool surface which can be defined as a layer between 10^{-2} mm and
 138 10^{-6} mm constitutes a preferred zone for plasticity and damage mechanisms. This
 139 can be explained by various phenomena like wear, shear strain and thermomechanical
 140 fatigue in coupling with oxydation when tools are working at high temperature.
 141 In order to investigate the influence of surface and subsurface properties on the
 142 mechanical behavior of X38CrMoV5-1 steel, a servo-hydraulic tensile test machine,
 143 with a nominal force of $20kN$ which was previously adapted to fretting fatigue tests,
 144 is used [52]. It is combined with a secondary axis with a nominal force of $25 kN$
 145 allowing to apply a transverse compressive loading to the sample by the use of cylin-
 146 drical pins. A back and forth axial displacement u controlled test is combined with
 147 a transverse loading/unloading force F as illustrated in Fig. 3. Hence, a surface
 148 with microstructural properties similar to those observed at the die surface during
 149 forging is obtained.

150

151 Such subsurface/surface mechanical and microstructural characteristics are achieved
 152 by applying high levels of loading. A limited number of cycles is enough to promote

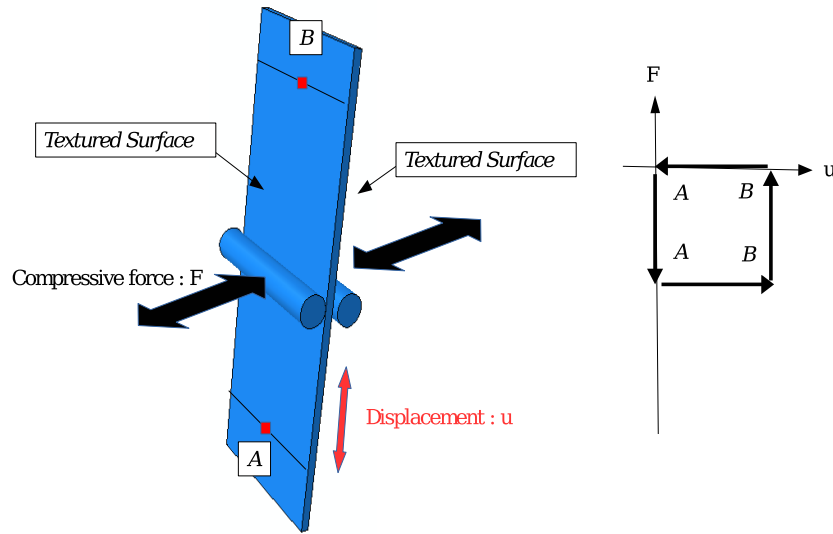


Figure 3: Experimental conditions of the surface generation process. Remark: the specimen is only hold by the movable actuator at one of its edges while the other is totally free to move.

153 inelastic flow. The tests use rectangular samples (270 mm long and 20 mm wide)
 154 with 1 mm thickness. Fig. 4 illustrates the SEM observation of the surface. In
 155 this case, 22 cycles of loading (forth axial displacement u from A to B) / unload-
 156 ing (back axial displacement u from B to A) are performed as shown in Fig. 3,
 157 with a maximal force of $F = 9.8 \text{ kN}$. EBSD analysis of a selected area, with a
 158 frame of $370 \times 270 \mu\text{m}^2$ shows a significant gradient of the morphological texture,
 159 in-depth from the surface. In such zones, it is very difficult to identify a consistent
 160 set of Kikuchi lines for properly indexing the highly elongated grains. Both SEM
 161 and EBSD investigations have revealed a mechanically affected zone of about $65 \mu\text{m}$.
 162

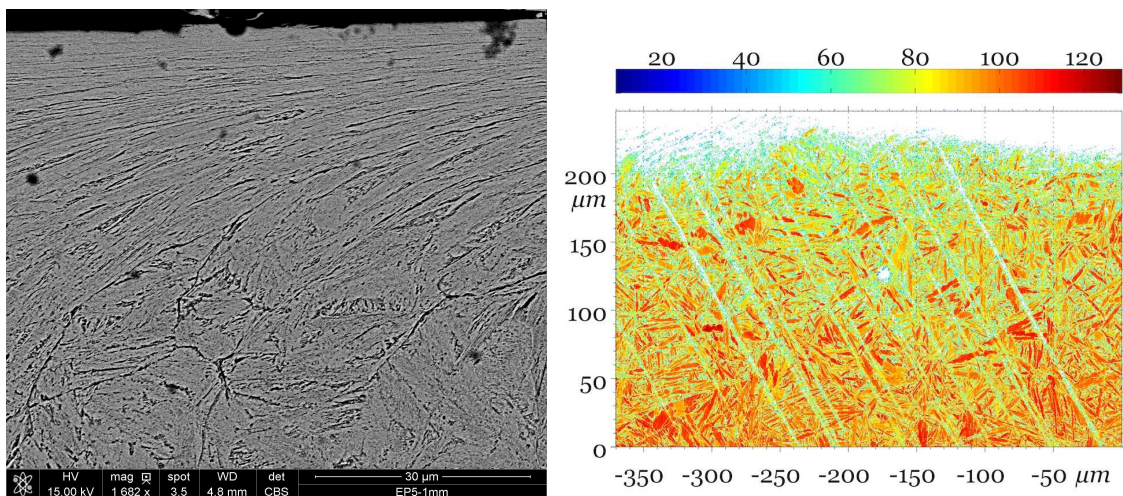


Figure 4: Surface analysis by SEM Observations and EBSD measurements

163 *2.3. In situ analysis of the local behavior*

164 The specimen are machined from the previous sheet by Electrical Discharge Ma-
 165 chining (EDM) such that the affected zone is kept on the gauge length as illustrated
 166 in Fig. 5. The tensile tests are conducted on a Instron servo-electric testing machine
 167 with a nominal force of 30 kN . The local strain measurement is done by using a
 168 Keyence optical microscope with a magnification factor of 1000. It is placed on a
 169 $x - y - z$ moving table for a very high accurate positioning of the microscope lens.
 170 An Area of Interest (AoI) of about $500 \times 500 \mu m^2$ is selected for in-situ measure-
 171 ments during tensile loading. Digital images of 1600×1200 pixels are captured.
 172 The martensitic microstructure is used as a natural speckle pattern. Moreover, the
 173 global strain is measured by a classical MTS extensometer with a gauge length of
 174 12.5 mm. It is placed beside the AoI (see Fig. 5). It should be emphasized that
 175 both sides of the specimen after EDM and the highly deformed surface (see Fig. 5)
 176 are slightly polished to reduce the eventual surface cracks. Care is taken to avoid
 177 and eliminate totally the textured surface.

178

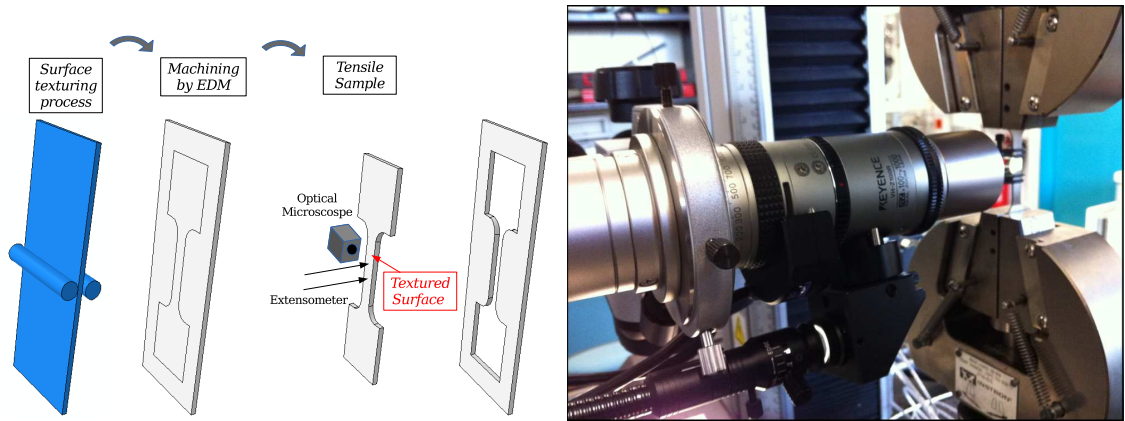


Figure 5: In-situ analysis of the deformation maps under monotonic loading by using Digital Image Correlation (DIC) technique

179 *2.4. RVE definition*

180 These measurements are used to assess the size of the RVE adapted to the
 181 X38CrMoV5-1 microstructure [53]. A preliminary tensile test is performed on a
 182 sample having a surface without any prior texturing. A tensile ductility of 8.5%
 183 is obtained with the global extensometer measurement. Several AoI are defined:
 184 $400 \times 400 \mu m^2$ (Z_1), $300 \times 300 \mu m^2$ (Z_2), $200 \times 200 \mu m^2$ (Z_3), $150 \times 150 \mu m^2$ (Z_4)
 185 and $100 \times 100 \mu m^2$ (Z_5). A mean spatial strain field of these AoI is calculated and
 186 compared with the global strain measured by the extensometer. Based on the mean
 187 strain calculated for each AoI, it is concluded that the Zone 5 underestimates the
 188 global strain measured by extensometer. On the contrary, Zones 3 and 4 can be
 189 considered as a RVE since the mean strain obtained is similar to the global strain
 190 (see Fig. 6). The relative local ductility given by the equation $\delta = (A_Z^{global} - A_Z^{AoI})$
 191 is reported in Table 2 where A_Z^{AoI} is the ductility calculated in each AoI and A_Z^{global}
 192 is the global ductility.

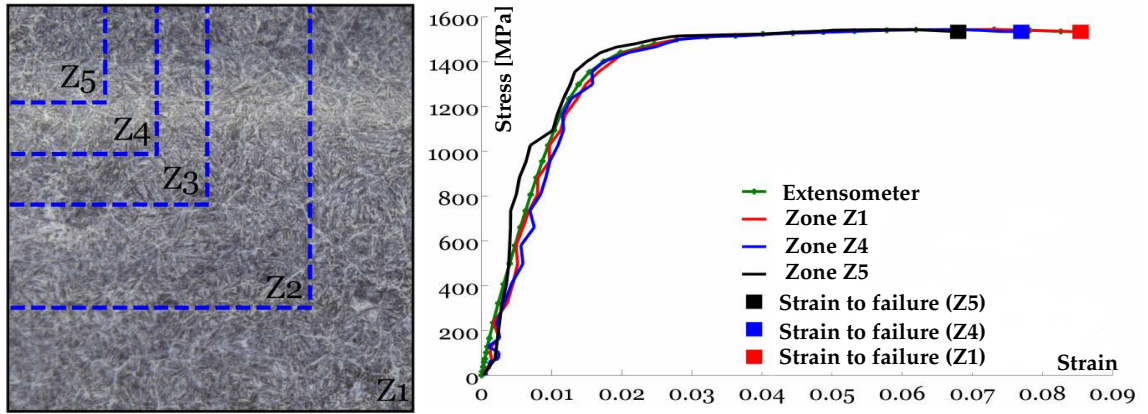


Figure 6: Estimation of the RVE size by using DIC technique and by comparison with the strain provided by the extensometer

Table 2: Gaps between the deformation to failure given by the extensometer and for each considered AoI

AoI	Z ₁	Z ₂	Z ₃	Z ₄	Z ₅
δ [%]	+ 3	+ 3	+ 3	- 9.41	- 20.09

193 *2.5. Tensile tests conducted on textured surface*

194 As an example, in Fig. 7, three strain fields are shown at various macroscopic
 195 strain levels (0.5%; 1%; 3%). The major strain field evolution is analyzed for each
 196 image. For a global 0.5 % elastic strain, a local major strain of 2.5% is calculated
 197 by DIC. Thus, a local plastic behavior occurs even if the macroscopic behavior
 198 remains elastic. Deformation seems to be initiated at the PAG boundaries and also
 199 is dependent on their orientations. At a global strain level of 1% and 3%, the strain
 200 is significant and seems to be localized at $\pm 45^\circ$ with respect to the tensile axis.
 201 Previous investigations performed on X38CrMoV5-1 tool steel [54] have shown an
 202 important plastic flow at the interface between the textured surface/subsurface and
 203 the bulk. This plasticity is localized at the boundaries of PAG and is responsible
 204 for micro voids initiation. This phenomenon causes the failure by decohesion at
 205 PAG and lath boundaries. It can explain the damage initiation at the subsurface of
 206 the material. The local strain field with the band at $\pm 45^\circ$ may be related to this
 207 mechanism.

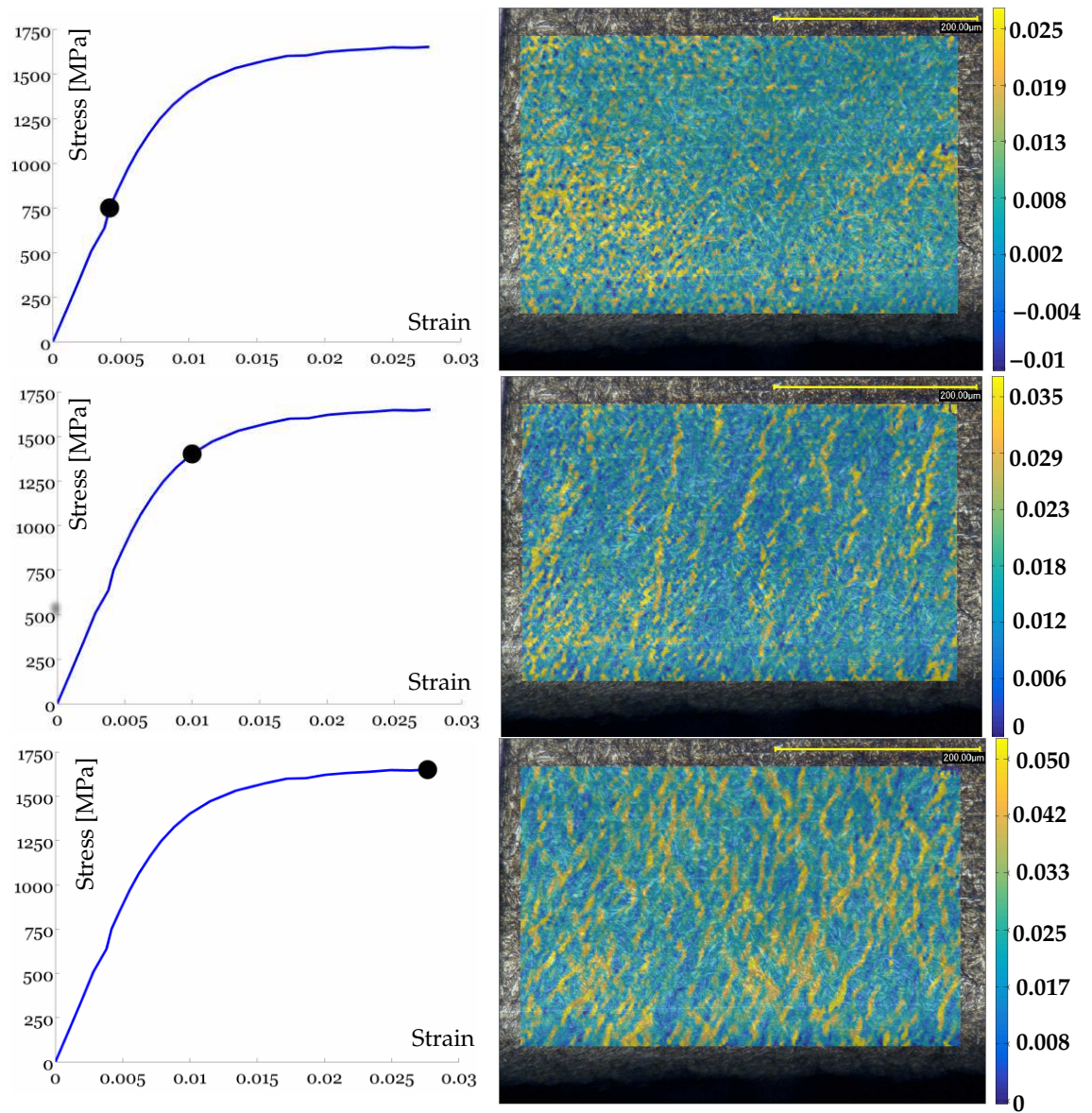


Figure 7: Major stain measurements provided by DIC technique at different macroscopic deformations (0.5%; 1%; 3%)

208 3. Multi-scale behavior modeling

209 In the present investigation, the multi-scale approach is based on the behavior
 210 model proposed by Meric and Cailletaud [34, 35], this approach satisfies the require-
 211 ments of the thermodynamics of irreversible processes [6, 23]. In this theoretical
 212 framework, the state laws or thermodynamic potentials can be written at different
 213 scales. The local behavior equations are formulated at the microscopic scale consid-
 214 ering the slip systems. The macroscopic RVE, previously defined, corresponds to a
 215 volume of $150 \times 150 \times 50 \mu m^3$. Inbetween these two scales, a mesoscopic scale corre-
 216 sponding to a martensitic lath is assumed. The martensitic lath blocks in a PAG are
 217 defined as an intermediate scale between the microscopic and the macroscopic scales.
 218 This micro-meso-macro approaches leads to define a multi-scale modeling and are
 219 governed by scale transition rules presented hereafter. Many works in the multi scale
 220 approaches using crystal plasticity modeling employ a finite strain (large strain) for-
 221 mulation [55, 56]. Nevertheless, bodies in relative movements (forging tool or pin on
 222 disc testing ...) are subjected to cumulative plastic straining with small cyclic strain
 223 ranges achieving definitively to high strain levels. Therefore, in the present study,
 224 a modeling framework based on small strains assumption is addressed. However, a
 225 finite strain approach is carried out and reported in [37].

226 3.1. Constitutive Equations

227 The Helmholtz potential energy density per unit mass usually defined at the
 228 macroscopic scale can also be considered as a potential given as the sum of free
 229 energies at the mesoscopic scale.

$$\varrho\Psi = \varrho\Psi_e\left(\left\langle\tilde{\boldsymbol{\varepsilon}}_e\right\rangle_{\mathcal{V}}\right) + \varrho\Psi_{in}(q_i) = \sum_{i=1}^N \left(\varrho\Psi_e^i(\tilde{\boldsymbol{\varepsilon}}_e) + \varrho\Psi_{in}^i(\rho_s, \alpha_s) \right) \quad (1)$$

230 where ϱ is the material density, N is the lath number in \mathcal{V} , $\left\langle\tilde{\boldsymbol{\varepsilon}}_e\right\rangle_{\mathcal{V}}$ the average
 231 elastic strain tensor in \mathcal{V} and q_i the internal variables including the isotropic ρ_s and
 232 kinematic α_s hardening variables resolved on each slip system s .

233 As mentioned earlier, small deformation conditions and an additive strain parti-
 234 tion $\tilde{\boldsymbol{\varepsilon}} = \tilde{\boldsymbol{\varepsilon}}_e + \tilde{\boldsymbol{\varepsilon}}_{in}$ are assumed. Moreover, a linear isotropic behaviour is considered.
 235 Therefore, the elasticity tensor is described by two parameters that are macroscopic
 236 Young modulus E and Poisson ratio ν .

237 In Eq. 1, the non linear Helmholtz free energy Ψ_{in}^i , for a given lath i , is associated
 238 to the non linear part of the behavior at the mesoscopic scale by considering the
 239 hardening variables formulated at a microscopic scale.

$$\varrho\Psi_{in}^i(\rho^s, \alpha^s) = \frac{1}{2}C \sum_{s=1}^{N_s} \alpha^{s2} + \frac{1}{2}bQ \sum_{s=1}^{N_s} \sum_{r=1}^{N_s} h^{sr} \rho^s \rho^r \quad (2)$$

C and Q are material parameters related to kinematic and isotropic hardening
 respectively. b is the isotropic hardening rate parameter and N_s is the number of
 slip systems potentially activated. For BCC crystal, the number of slip systems is
 given by slip planes $\{1\ 1\ 0\}$, $\{1\ 1\ 2\}$, $\{1\ 2\ 3\}$ and slip directions $\langle 1\ 1\ 1 \rangle$. It confers

to the polycrystal 48 activable slip systems. In the present study, the deformation mechanisms related to easy glide and pencil glide mechanisms are considered to be predominant, e.g: $\{110\} \langle 111 \rangle$ and $\{112\} \langle 111 \rangle$ [57]. Therefore, the number of active slip systems is reduced and only 24×24 interaction matrix $\tilde{\mathbf{h}}$ including 8 coefficients h_i symmetrically allocated [8, 58, 59] is required (Eq. A.1 into the appendix section). The previous slip system families are given by the Schmid-Boas notations in Eq. A.1. The link between Miller indexes and Schmid-Boas system is provided in Tab. A.8 shown into the same appendix section. The macroscopic Cauchy stress $\tilde{\Sigma} = \langle \tilde{\sigma} \rangle_{\mathcal{V}}$ is the average stress tensor in \mathcal{V} (Eq. 3), it is obtained by derivation of the Helmotz free energy (see Eq. 1 and Eq. 2).

$$\tilde{\Sigma} = \langle \tilde{\sigma} \rangle_{\mathcal{V}} = \varrho \frac{\partial \Psi_e \left(\langle \tilde{\epsilon}_e \rangle_{\mathcal{V}} \right)}{\partial \langle \tilde{\epsilon}_e \rangle_{\mathcal{V}}} = \tilde{\Lambda} : \langle \tilde{\epsilon}_e \rangle_{\mathcal{V}} \quad (3)$$

The associated variables related to the isotropic and kinematic hardening at the microscopic scale are described in Eq.4 and 5.

$$r^s = \varrho \frac{\partial \Psi_{in}^i(\rho^s, \alpha^s)}{\partial \rho^s} = bQ \sum_{r=1}^{N_s} h^{sr} \rho^r \quad (4)$$

$$\chi^s = \varrho \frac{\partial \Psi_{in}^i(\rho^s, \alpha^s)}{\partial \alpha^s} = C\alpha^s \quad (5)$$

240 Similarly, the evolution equations are obtained at the macroscopic scale by defin-
 241 ing a viscoplastic potential Ω at the mesoscopic scale. This global potential being
 242 the sum of the partial potentials Ω_s obtained at the microscopic scale (Eq. 6).

$$\Omega = \sum_{s=1}^{N_s} \Omega_s = \sum_{s=1}^{N_s} \frac{K}{n+1} \left\langle \frac{f^s}{K} \right\rangle^{n+1} \quad (6)$$

243 where K and n are parameters related to the material viscosity and f^s is the yield
 244 function of the slip system s given by Eq. 7.

$$f^s = |\tau^s - \chi^s| - r^s - \tau_0^s \quad (7)$$

245 where τ^s and τ_0^s are respectively the resolved shear stress and the critical resolved
 246 shear stress.

247 This approach can be classified in the frame of non associated models [6] since
 248 it is defined by two functions, the function f (Eq. 7) for the elasticity domain and
 249 the flow potential given by F (Eq. 8).

$$F^s = f^s + b\rho^s r^s + d\alpha^s \chi^s \quad (8)$$

250 where d is a material parameter related to the kinematic variable.

251 From Eq. 6 and 8, the evolution equations of internal variables (Eq. 9-11) are
 252 obtained as:

$$\dot{\gamma}^s = \dot{\lambda}^s \frac{\partial F^s}{\partial \tau^s} = \left\langle \frac{f^s}{K} \right\rangle^n \text{sign}(\tau^s - \chi^s) = \dot{v}^s \text{sign}(\tau^s - \chi^s) \quad (9)$$

$$\dot{\rho}^s = -\dot{\lambda}^s \frac{\partial F^s}{\partial r^s} = (1 - b\rho^s) \dot{v}^s \quad (10)$$

$$\dot{\alpha}^s = -\dot{\lambda}^s \frac{\partial F^s}{\partial \chi^s} = \left(\text{sign}(\tau^s - \chi^s) - d\alpha^s \right) \dot{v}^s \quad (11)$$

where $\dot{\lambda}^s$ is a viscoplastic multiplier which is derivated from the viscoplastic potential Ω_s at the microscopic scale (Eq. 12)

$$\dot{\lambda}^s = \frac{\partial \Omega_s}{\partial f^s} = \dot{v}^s \quad (12)$$

253 The Schmid law (Eq. 13) and the yield function (Eq. 7) define the mesoscopic
 254 non linear strain rate (Eq. 14).

$$\tau^s = \underset{\sim}{\boldsymbol{\sigma}} : \text{sym}(\underset{\sim}{\boldsymbol{l}}^s \otimes \underset{\sim}{\boldsymbol{n}}^s) \quad (13)$$

$$\underset{\sim}{\dot{\boldsymbol{\epsilon}}}^{in} = \frac{\partial \Omega}{\partial \underset{\sim}{\boldsymbol{\sigma}}} = \sum_{s=1}^{N_s} \frac{\partial \Omega_s}{\partial \underset{\sim}{\boldsymbol{\sigma}}} = \sum_{s=1}^{N_s} \dot{\lambda}^s \frac{\partial f^s}{\partial \underset{\sim}{\boldsymbol{\sigma}}} = \sum_{s=1}^{N_s} \dot{\gamma}^s \text{sym}(\underset{\sim}{\boldsymbol{n}}^s \otimes \underset{\sim}{\boldsymbol{l}}^s) \quad (14)$$

255 where $\underset{\sim}{\boldsymbol{n}}^s$ is the slip plane normal vector and $\underset{\sim}{\boldsymbol{l}}^s$ the slip direction in this plane.

256 The state laws (Eq. 4 and 5) and the evolution equations (Eq. 9-13) express the
 257 intrinsic dissipation Θ as:

$$\begin{aligned} \Theta &= \underset{\sim}{\boldsymbol{\sigma}} : \underset{\sim}{\dot{\boldsymbol{\epsilon}}}^{in} - \sum_{s=1}^{N_s} \chi^s \dot{\alpha}^s - \sum_{s=1}^{N_s} r^s \dot{\rho}^s \\ &= \sum_{s=1}^{N_s} \left(\tau^s \dot{\gamma}^s - \chi^s \left(\text{sign}(\tau^s - \chi^s) - d\alpha^s \right) \dot{v}^s - r^s (1 - b\rho^s) \dot{v}^s \right) \\ &= \sum_{s=1}^{N_s} \left(f^s + \tau_0^s + \frac{d}{C} (\chi^s)^2 + br^s \rho^s \right) \end{aligned} \quad (15)$$

258 Table 3 summarizes the equations set.

259 3.2. Strategies for identification of the model parameters

260 As observed in the above, DIC measurements reveal heterogeneous strain fields
 261 distribution in tensile tests. Therefore, a straightforward identification of the ma-
 262 terial paramters associated to the chosen model is impossible. Indeed a full field
 263 approach requires the generation of the virtual microstructure associated with the

Table 3: Constitutive equations of the model of Meric and Cailletaud

Strain decomposition	$\underline{\boldsymbol{\varepsilon}} = \underline{\boldsymbol{\varepsilon}}^e + \underline{\boldsymbol{\varepsilon}}^{in}$	
Schmid law	$\tau_s = \underline{\boldsymbol{\sigma}} : \text{sym}(\underline{\boldsymbol{l}}^s \otimes \underline{\boldsymbol{n}}^s)$	
Microscopic flow rule	$\dot{\nu}^s = \left\langle \frac{ \tau^s - \chi^s - r^s - \tau_0^s}{K} \right\rangle^n$	$\dot{\gamma}^s = \dot{\nu}^s \text{sign}(\tau^s - \chi^s)$
Mesoscopic flow rule	$\underline{\dot{\boldsymbol{\varepsilon}}}^{in} = \sum_{s=1}^{N_s} \dot{\gamma}^s \text{sym}(\underline{\boldsymbol{n}}^s \otimes \underline{\boldsymbol{l}}^s)$	
Kinematic hardening	$\chi^s = C\alpha^s$	$\dot{\alpha}^s = \dot{\gamma}^s - d\alpha^s \dot{\nu}^s$
Isotropic Hardening	$r^s = bQ \sum_{r=1}^{N_s} h^{sr} \rho^r$	$\dot{\rho}^s = (1 - b\rho^s) \dot{\nu}^s$
Intrinsic dissipation	$\Theta = \underline{\boldsymbol{\sigma}} : \underline{\dot{\boldsymbol{\varepsilon}}}^{in} - \sum_{s=1}^{N_s} \chi^s \dot{\alpha}^s - \sum_{s=1}^{N_s} r^s \dot{\rho}^s$	

264 knowledge of various slip systems and crystallographic orientations. In addition,
 265 the mechanical tests should be combined with high resolution EBSD measurements.
 266 Consequently, the optimisation method becomes very time consuming which lead
 267 to consider a mean field approach. As mentionned previously, the Berveiller-Zaoui
 268 model [18] and β -model of Pilvin and Cailletaud [10, 19] are combined for the pa-
 269 rameters identification purpose. This latter is relevant for modelling the behavior
 270 of softening materials as it is observed during the cyclic behavior of hot work tool
 271 steels [60]. For Berveiller-Zaoui model, the localization rule of the stress tensor is
 272 given by Eq. 16.

$$\begin{aligned}
 \underline{\boldsymbol{\sigma}}^\varphi &= \underline{\boldsymbol{\Sigma}} + 2\mu\alpha(1 - \beta) : (\underline{\boldsymbol{E}}^p - \underline{\boldsymbol{\varepsilon}}^{\varphi,p}) \\
 \text{with: } \frac{1}{\alpha} &= 1 + \frac{3}{2}\mu \frac{E_{eq}^p}{\Sigma_{eq}} \quad \text{and: } \beta = \frac{2(4 - 5\nu)}{15(1 - \nu)}
 \end{aligned} \tag{16}$$

273 where $\underline{\boldsymbol{\sigma}}^\varphi$ and $\underline{\boldsymbol{\Sigma}}$ are respectively the stresses at the mesoscopic/lath and macro-
 274 scopic scales, ν is the Poisson ratio, μ the shear modulus and α stands for a non
 275 linear accommodation parameter whose formulation is a function of the von Mises
 276 equivalent inelastic strain E_{eq}^p and stress Σ_{eq} at the macroscopic scale.

277 In β -model (Eq. 17), the transition is given as a difference between a global $\underline{\boldsymbol{B}}$
 278 and local $\underline{\boldsymbol{\beta}}^\varphi$ variables in order to describe the non linear accommodation whereas
 279 the Berveiller-Zaoui model considers a difference between a global $\underline{\boldsymbol{E}}^p$ and local $\underline{\boldsymbol{\varepsilon}}^{\varphi,p}$
 280 inelastic strains.

$$\begin{aligned}
 \underline{\boldsymbol{\sigma}}^\varphi &= \underline{\boldsymbol{\Sigma}} + 2\mu(1 - \beta) : (\underline{\boldsymbol{B}} - \underline{\boldsymbol{\beta}}^\varphi) \\
 \text{with: } \underline{\boldsymbol{B}} &= \left\langle \underline{\boldsymbol{\beta}}^\varphi \right\rangle = \sum_{\varphi} f_{\varphi} \underline{\boldsymbol{\beta}}^\varphi
 \end{aligned} \tag{17}$$

281 Moreover, $\underline{\boldsymbol{\beta}}^\varphi$ presents a non linear evolution with respect to inelastic strain. This
 282 evolution law (Eq. 18) can be written under a Armstrong-Frederick form [5, 6]. Thus,
 283 this transition rule can be extended to complex loading paths like cyclic behavior.

$$\dot{\tilde{\beta}}^\varphi = \dot{\tilde{\epsilon}}^{p,\varphi} - D\tilde{\beta}^\varphi \dot{\tilde{\epsilon}}_{eq}^{p,\varphi} \quad (18)$$

284 where $\dot{\tilde{\epsilon}}_{eq}^{p,\varphi}$ is the equivalent inelastic strain rate at the mesoscopic scale. The
 285 β -model is reliable for both monotonic and cyclic loadings but requires the identifi-
 286 cation of an additional coefficient D .

287 The parameters identification is based on experimental tensile and cyclic strain-
 288 controlled tests at room temperature. A servo-hydraulic testing machine and Testar
 289 2S controller are used. The push-pull tests with a strain rate of $10^{-2}s^{-1}$ exhibit a
 290 cyclic softening from the first cycle to the failure which is a well known behavior
 291 of martensitic hot work tool steels [50, 61, 62]. Several strain ranges are examined
 292 under two strain ratios $R_\epsilon = \{-1, 0\}$ (Table 4).

Table 4: Tensile and cyclic test conditions, $\dot{\epsilon} = 10^{-2}s^{-1}$

Test number	tensile 1	cyclic 1	cyclic 2	cyclic 3	cyclic 4
Strain range	0 – 10%	$\pm 0.8\%$	$\pm 0.9\%$	$\pm 1.1\%$	0 – 1.5%

293 The identification process of the model parameters contains several steps. First,
 294 by assuming an isotropic behavior, the elasticity tensor $\mathbf{\Lambda}$ is identified using the
 295 Young modulus E and the Poisson ratio ν . As at room temperature, the material
 296 is not sensitive to strain rate, the viscous parameters K and n are set to provide
 297 a rate-independent model response which can be considered as a limiting case of
 298 classical viscoplasticity. The kinematic and isotropic hardening coefficients and the
 299 transition rule parameter are identified from experimental tests. For this purpose,
 300 the following sequential stages (simulation and optimisation) are undertaken using
 301 the Zset solution software [63]:

- 302 • transition rule parameter, kinematic hardening and critical resolved shear
 303 stress are identified using the tensile curve,
- 304 • then the values of the kinematic hardening coefficients are refined using the
 305 stabilized cycles of the different cyclic tests (see table 4),
- 306 • isotropic hardening parameters are identified by fitting the both tensile and
 307 cyclic experiments,
- 308 • the interaction matrix coefficients are identified using the tensile test. In this
 309 case, the following constraints (see Eq. 19) are assumed according to the work
 310 of Hoc and Forest for BCC crystals [59]:

$$h_8 \leq h_2 \leq h_3 \leq h_5 \leq h_4 \leq h_1 \leq h_6 \leq h_7 \quad (19)$$

311 The interactions between slip systems $\{110\} \langle 111 \rangle$ and $\{112\} \langle 111 \rangle$ are
 312 classified in different types. They can belong to the same system (h_1 and
 313 h_8), to colinear system (h_2, h_3 and h_6) or to non-colinear system (h_5, h_4 and
 314 h_7). Interactions between same or colinear slip systems of the family $\{110\}$

Table 5: Material parameters

Elasticity [GPa, GPa, \emptyset]			Viscosity [unitless, MPa.s ⁻ⁿ]				Kinematic hardening [GPa, \emptyset]				
Young Modulus E	Shear modulus μ	Poisson ratio ν	n	K			C	d			
208	80	0.3	15	4			495	1700			
Isotropic hardening [MPa, MPa, \emptyset]		Transition rule [\emptyset]	Interaction matrix coefficients [\emptyset]								
τ_0^s	Q	b	D	h_1	h_2	h_3	h_4	h_5	h_6	h_7	h_8
372	-10	1.05	15	1.1	0.7	0.9	1.0	0.9	1.2	1.3	0.7

315 $\langle 111 \rangle$ are assumed smaller than interactions between colinear slip systems
 316 not belonging to the same family, this latter being smaller than interactions
 317 between non colinear slip systems itself smaller than interactions between non
 318 colinear system of the family $\{110\}$ $\langle 111 \rangle$. Lastly, interactions between slip
 319 systems of the family $\{112\}$ $\langle 111 \rangle$ are assumed greater than interactions
 320 between slip system of the family $\{110\}$ $\langle 111 \rangle$.

- 321 • Model validation by simulation of the tensile test using the transition rule of
 322 Berveiller-Zaoui.

323 The results of the identification process are illustrated in Table 5. The compari-
 324 son between the results provided by the Meric-Cailletaud model using the β -model
 325 transition rule and our experiments are given for cyclic and tensile loading paths
 326 (Fig. 8).

327

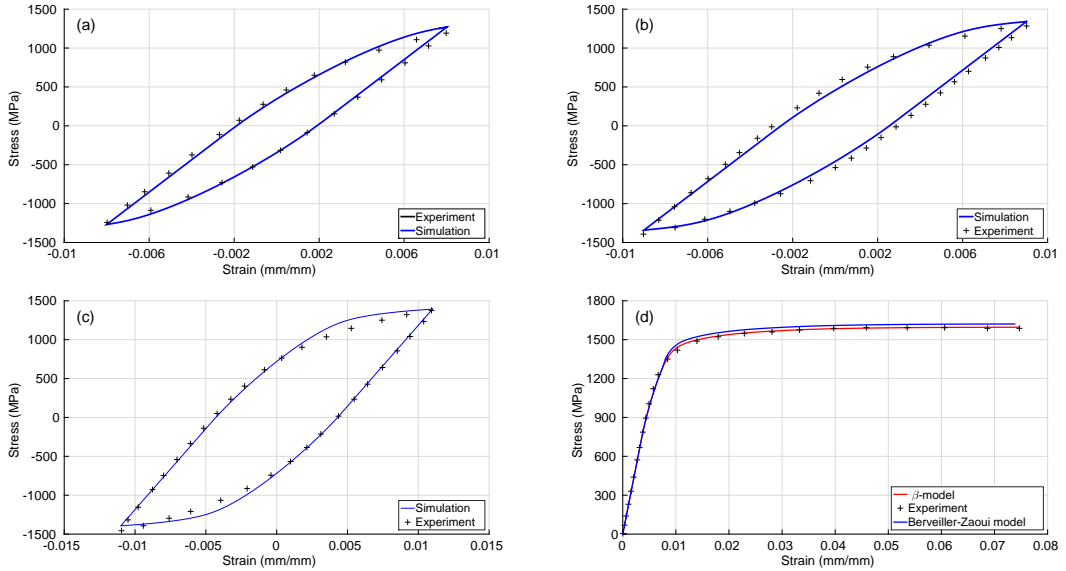


Figure 8: Comparison between computed strain-stress curve provided and experiment for the stabilized cycle (a-c); test *cyclic1* (a); test *cyclic2* (b); test *cyclic3* (c); and for test *tensile1* using Berveiller-Zaoui and β models (d)

328 4. Numerical simulations

329 4.1. Finite Element implementation of the constitutive equations

330 A lot of investigations deals with the FE implementation of a multiscale ap-
 331 proach [4, 64–69]. In the present work, the rate tangent modulus method [15, 16]
 332 is used to implement the multiscale constitutive equations. The method consists in
 333 a direct resolution scheme and is based on a predictor/corrector algorithm of Simo
 334 and Hughes [70] where the Cauchy stress $\underline{\sigma}$ is written at the mesoscopic scale.

$$\underline{\sigma} = \underline{\mathbf{A}} : \left(\underline{\varepsilon} - \underline{\varepsilon}^{in} \right) \quad (20)$$

From Eq. 20 and using Eq. 14, Eq. 21 is obtained.

$$\underline{\dot{\sigma}} = \underline{\mathbf{A}} : \left(\underline{\dot{\varepsilon}} - \sum_{s=1}^{N_s} \dot{\gamma}^s \text{sym}(\underline{l}^s \otimes \underline{n}^s) \right) \quad (21)$$

The incremental shear strain $\Delta\gamma^s$ on a prescribed system s at time t is defined by Eq. 22, where Δt is the time increment.

$$\Delta\gamma^s = \gamma_{t+\Delta t}^s - \gamma_t^s \quad (22)$$

Interpolation versus time can be expressed as Eq. 23.

$$\Delta\gamma^s = \left((1 - \theta)\dot{\gamma}_t^s + \theta\dot{\gamma}_{t+\Delta t}^s \right) \Delta t \quad (23)$$

335 By Taylor expansion of $\dot{\gamma}_{t+\Delta t}^s$, Eq. 24 then Eq. 25 can be achieved. In each slip
 336 system s , the shear strain rate $\dot{\gamma}^s$ is considered as the integration variable.

$$\dot{\gamma}_{t+\Delta t}^s = \dot{\gamma}_t^s + \left. \frac{\partial \dot{\gamma}^s}{\partial \tau^s} \right|_t \Delta\tau^s + \left. \frac{\partial \dot{\gamma}^s}{\partial r^s} \right|_t \Delta r^s + \left. \frac{\partial \dot{\gamma}^s}{\partial \chi^s} \right|_t \Delta\chi^s \quad (24)$$

$$\frac{\Delta\gamma^s}{\Delta t} = \dot{\gamma}_t^s + \theta \left. \frac{\partial \dot{\gamma}^s}{\partial \tau^s} \right|_t \Delta\tau^s + \theta \left. \frac{\partial \dot{\gamma}^s}{\partial r^s} \right|_t \Delta r^s + \theta \left. \frac{\partial \dot{\gamma}^s}{\partial \chi^s} \right|_t \Delta\chi^s \quad (25)$$

337 where $\Delta\tau^s$, Δr^s et $\Delta\chi^s$ are respectively the resolved shear stress, isotropic hard-
 338 ening and kinematic hardening increment acting on slip system s . These increments
 339 can be determined by using the constitutive equations (see Eq. 26, 27 and 28).

$$\Delta\tau^s = \left(\underline{\mathbf{A}} : \text{sym}(\underline{l}^s \otimes \underline{n}^s) \right) : \left(\underline{\Delta\varepsilon} - \sum_{r=1}^{N_s} \Delta\gamma^r \text{sym}(\underline{l}^r \otimes \underline{n}^r) \right) \quad (26)$$

$$\Delta r^s = bQ \sum_{r=1}^{N_s} h^{sr} (1 - b\rho^r) \Delta\gamma^r \text{sign}(\tau^r - \chi^r) \quad (27)$$

$$\Delta\chi^s = C\Delta\gamma^s - Cd\alpha^s \Delta\gamma^s \text{sign}(\tau^s - \chi^s) \quad (28)$$

340 Eq. 29 is obtained by introducing the previous equations into Eq. 25:

$$\begin{aligned}
\frac{\Delta\gamma^s}{\Delta t} &= \dot{\gamma}_t^s + \theta \left. \frac{\partial \dot{\gamma}^s}{\partial \tau^s} \right|_t \left(\underline{\mathbf{A}} : \text{sym}(\underline{\mathbf{l}}^s \otimes \underline{\mathbf{n}}^s) \right) : \left(\Delta \underline{\boldsymbol{\varepsilon}} - \sum_{r=1}^{N_s} \Delta \gamma^r \text{sym}(\underline{\mathbf{l}}^r \otimes \underline{\mathbf{n}}^r) \right) \\
&+ \theta \left. \frac{\partial \dot{\gamma}^s}{\partial r^s} \right|_t \left(bQ \sum_{r=1}^{N_s} h^{sr} (1 - b\rho_t^r) \Delta \gamma^r \text{sign}(\tau^r - \chi^r) \right) \\
&+ \theta \left. \frac{\partial \dot{\gamma}^s}{\partial \chi^s} \right|_t \left(C \Delta \gamma^s - C d \alpha_t^s \Delta \gamma^s \text{sign}(\tau^s - \chi^s) \right)
\end{aligned} \tag{29}$$

341 Therefore, Eq. 29 can be expressed as a linear system (see Eq. 30) where the
342 components of unknown vector $\underline{\Delta \boldsymbol{\gamma}}$ correspond to the shear strain increment for all
343 slip systems.

$$\underline{\mathbf{A}} \cdot \underline{\Delta \boldsymbol{\gamma}} = \underline{\mathbf{b}} \tag{30}$$

with:

$$\begin{aligned}
\underline{\mathbf{A}} &= A^{sr} = \delta^{sr} + \Delta t \theta \left. \frac{\partial \dot{\gamma}^s}{\partial \tau^s} \right|_t \left(\underline{\mathbf{A}} : \text{sym}(\underline{\mathbf{l}}^s \otimes \underline{\mathbf{n}}^s) \right) : \left(\text{sym}(\underline{\mathbf{l}}^r \otimes \underline{\mathbf{n}}^r) \right) \\
&- \Delta t \theta \left. \frac{\partial \dot{\gamma}^s}{\partial r^s} \right|_t bQ h^{sr} (1 - b\rho^r) \text{sign}(\tau^s - \chi^s) \\
&- \Delta t \theta \left. \frac{\partial \dot{\gamma}^s}{\partial \chi^s} \right|_t \left(\delta^{sr} C - \delta^{sr} C d \alpha^s \text{sign}(\tau^s - \chi^s) \right) \\
\underline{\Delta \boldsymbol{\gamma}} &= \Delta \gamma^r; \quad \underline{\mathbf{b}} = b^s = \Delta t \dot{\gamma}^s + \Delta t \theta \left. \frac{\partial \dot{\gamma}^s}{\partial \tau^s} \right|_t \left(\underline{\mathbf{A}} : \text{sym}(\underline{\mathbf{l}}^s \otimes \underline{\mathbf{n}}^s) \right) : \Delta \underline{\boldsymbol{\varepsilon}}
\end{aligned} \tag{31}$$

344 δ^{sr} is the Kronecker symbol and the derivative terms $\left. \frac{\partial \dot{\gamma}^s}{\partial \tau^s} \right|_t$, $\left. \frac{\partial \dot{\gamma}^s}{\partial r^s} \right|_t$ and $\left. \frac{\partial \dot{\gamma}^s}{\partial \chi^s} \right|_t$ can be
345 expressed using the constitutive laws of the Meric and Cailletaud model (see Eq.32).

$$\begin{aligned}
\left. \frac{\partial \dot{\gamma}^s}{\partial \tau^s} \right|_t &= \frac{n}{K^n} (|\tau^s - \chi^s| - r^s - \tau_0^s)^{n-1} \\
\left. \frac{\partial \dot{\gamma}^s}{\partial r^s} \right|_t &= -\frac{n}{K^n} (|\tau^s - \chi^s| - r^s - \tau_0^s)^{n-1} \text{sign}(\tau^s - \chi^s) \\
\left. \frac{\partial \dot{\gamma}^s}{\partial \chi^s} \right|_t &= -\frac{n}{K^n} (|\tau^s - \chi^s| - r^s - \tau_0^s)^{n-1}
\end{aligned} \tag{32}$$

346 By solving the linear system given by Eq. 30, $\Delta \gamma^s$ is calculated and the shear
347 strain rate $\dot{\gamma}^s = \frac{\Delta \gamma^s}{\Delta t}$ is assessed. As the *rate tangent modulus* method allows for
348 a direct solving, the calculated shear strain increment may be not reliable when
349 the time increment increases. Therefore this method is combined with a Newton
350 Raphson resolution using the value provided by *rate tangent modulus* method as
351 initial guess of the iterative algorithm. In the present investigation, an backward
352 Euler or fully implicit method ($\theta = 1$) is assumed (Eq. 33) [71].

$$\Delta\gamma^s - \Delta t \dot{\gamma}_{t+\Delta t}^s = 0 \quad (33)$$

353 The numerical integration of the above constitutive equations is implemented on
 354 ABAQUS/Standard. As implicit solving of the equilibrium equations is used, the
 355 Jacobian matrix $\mathcal{J} = \frac{\partial \Delta \boldsymbol{\sigma}}{\partial \Delta \boldsymbol{\varepsilon}}$ associated to the nonlinear system is assessed from Eq.
 356 21 (see Eq. 34).

$$\mathcal{J} = \frac{\partial \Delta \boldsymbol{\sigma}}{\partial \Delta \boldsymbol{\varepsilon}} = \frac{\partial \left[\boldsymbol{\Lambda} : \left(\Delta \boldsymbol{\varepsilon} - \sum_{s=1}^{N_s} \Delta \gamma^s \text{sym}(\underline{\mathbf{l}}^s \otimes \underline{\mathbf{n}}^s) \right) \right]}{\partial \Delta \boldsymbol{\varepsilon}} \quad (34)$$

$$= \boldsymbol{\Lambda} - \boldsymbol{\Lambda} : \left[\sum_{s=1}^{N_s} \frac{\partial \Delta \gamma^s}{\partial \Delta \boldsymbol{\varepsilon}} \otimes \text{sym}(\underline{\mathbf{l}}^s \otimes \underline{\mathbf{n}}^s) \right] \quad (35)$$

357 Hence, the term $\frac{\Delta \gamma^s}{\Delta \boldsymbol{\varepsilon}}$ can be easily formulated by Eq. 30.

$$\frac{\partial \Delta \gamma^r}{\partial \Delta \boldsymbol{\varepsilon}} = \boldsymbol{\Lambda}^{-1} \cdot \left[\Delta t \theta \frac{\partial \dot{\gamma}^s}{\partial \tau^s} \Big|_t \boldsymbol{\Lambda} : \text{sym}(\underline{\mathbf{l}}^s \otimes \underline{\mathbf{n}}^s) \right] \quad (36)$$

358 and by introducing Eq. 36 into Eq. 34, the final expression of \mathcal{J} is given by Eq. 37.

$$\mathcal{J} = \boldsymbol{\Lambda} - \sum_{r=1}^{N_s} \sum_{s=1}^{N_s} A^{rs,-1} \Delta t \theta \frac{\partial \dot{\gamma}^r}{\partial \tau^r} \Big|_t \left[\boldsymbol{\Lambda} : \text{sym}(\underline{\mathbf{l}}^r \otimes \underline{\mathbf{n}}^r) \right] \otimes \left[\boldsymbol{\Lambda} : \text{sym}(\underline{\mathbf{l}}^s \otimes \underline{\mathbf{n}}^s) \right] \quad (37)$$

359 4.2. Validation of the Finite Element implementation

360 The numerical implementation scheme is validated by comparison with the re-
 361 sults provided by Zset solution [35, 63]. The θ -method used in Zset solution (Eq.
 362 38), deduced from Eq. 33 is solved by a Newton-Raphson method.

$$K \left| \frac{\Delta \gamma^s}{\Delta t} \right|^{\frac{1}{n}} - \left(|(\tau^{s,t+\theta \Delta t} - \chi^{s,t+\theta \Delta t}) - r^{s,t+\theta \Delta t} - \tau_0^s| \right) = 0 \quad (38)$$

363 The validation procedure is performed on a single crystal stainless steel where
 364 the data are collected from [28]. It should be mentioned that the slip interaction
 365 matrix is formulated for a BCC structure ($h_i = 1; \forall i = 1, \dots, 8$). A 10 mm diameter
 366 and 20 mm length cylinder is considered. It is embedded on one side and undergone
 367 a tensile loading up to 4%. 8-node linear brick elements are used for the meshing,
 368 more than 400 elements are generated with a full integration. The comparison be-
 369 tween both approaches exhibits a good agreement (Fig. 9).

370

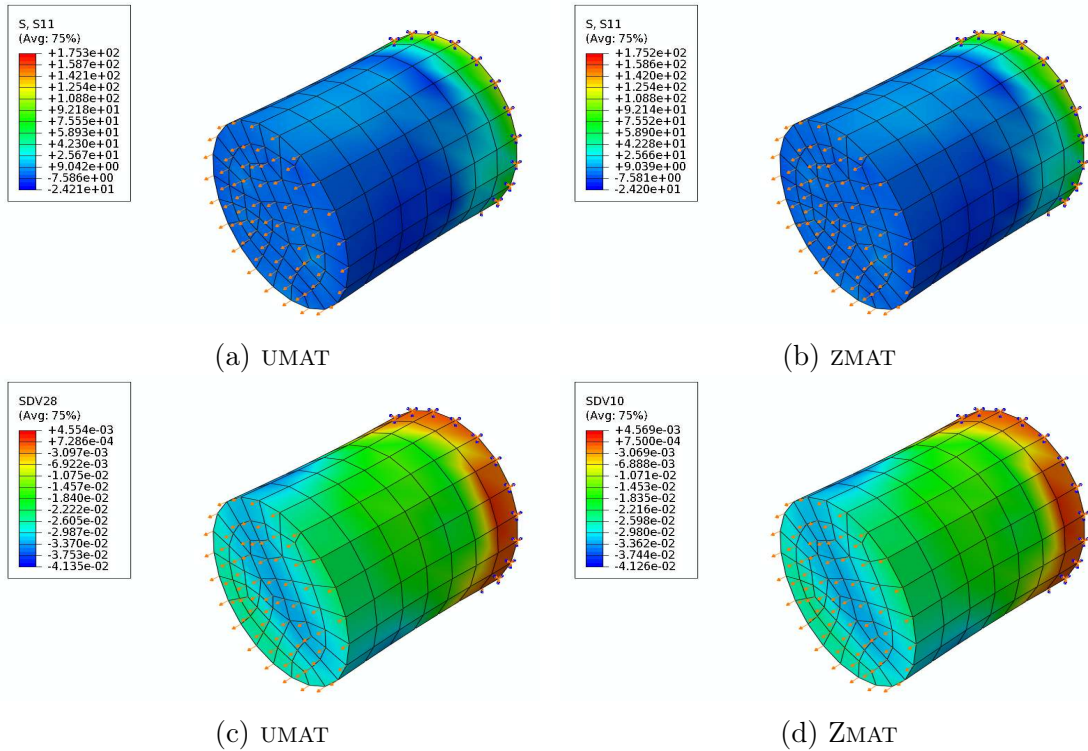


Figure 9: Comparison of the stress field (a-b) in the loading direction and the shear stress (c-d) of the Schmid-Boas slip system G1 (see Tab. A.8) obtained by the integration method developed in this work (a-c) and those provided by Zset Solution [63] (b-d)

371 4.3. Finite Element pre-processing

372 Voronoï cell tessellations are used to generate the virtual microstructure of X38CrMoV5-
 373 1 martensitic steel. The computational methodology consists in performing ordinary
 374 Voronoï tessellations [72, 73] in a spatial domain (REV) of $150 \times 150 \times 50 \mu\text{m}^3$. Tes-
 375 sellation generation is given by Neper software [40, 74]. 173 polycrystalline aggregates
 376 representing the potentials sites of the martensitic packets (First order Tessellation)
 377 are generated (Fig. 10a). Then, from this first order tessellation, starting from these
 378 sites, randomly oriented segments are generated where additional nucleation points
 379 are placed from which a second Voronoï tessellation is performed (second order Tes-
 380 sellation, Fig. 10b). 6 parallel laths are considered in each block except for one where
 381 only 2 laths are considered, achieving a total $N = 1034$ ($172 \times 6 + 2$) Voronoï cells.
 382 The Crystallographic orientations of the laths are not explicitly considered in the
 383 virtual microstructure. In fact, the laths are grouped in a parallel manner in each
 384 block and are randomly oriented from one to another block. PAGs are constituted
 385 of 4 packets of laths except for one PAG including only 2 laths achieving 44 PAG.

386
 387 Due to the relative motion between the surfaces of the tool and the part, a non
 388 isotropic microstructure (elongated PAG and laths) is generated close to the surface
 389 of the tool. For this purpose, the Voronoï cell centers related to the upper half
 390 of RVE are translated to represent elongated virtual microstructure (Fig.11a-11b).
 391 Furthermore, micro-hardness measurements reveal a hardening close to the free sur-
 392 face. This hardening is considered into the FE simulation by increasing the critical

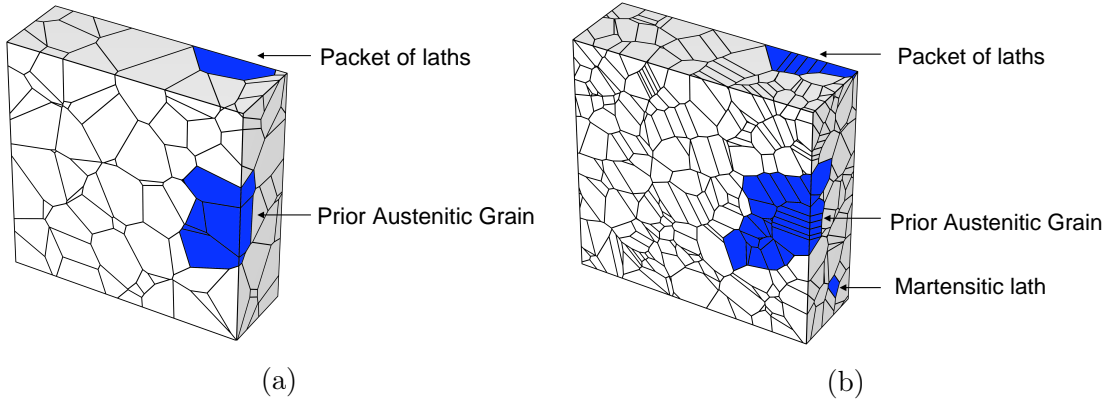


Figure 10: Virtual microstructure generation by Voronoï tessellations: first order tessellation (a); second order tessellation (b)

393 resolved shear stress in-depth from the surface (Fig. 11c).

394

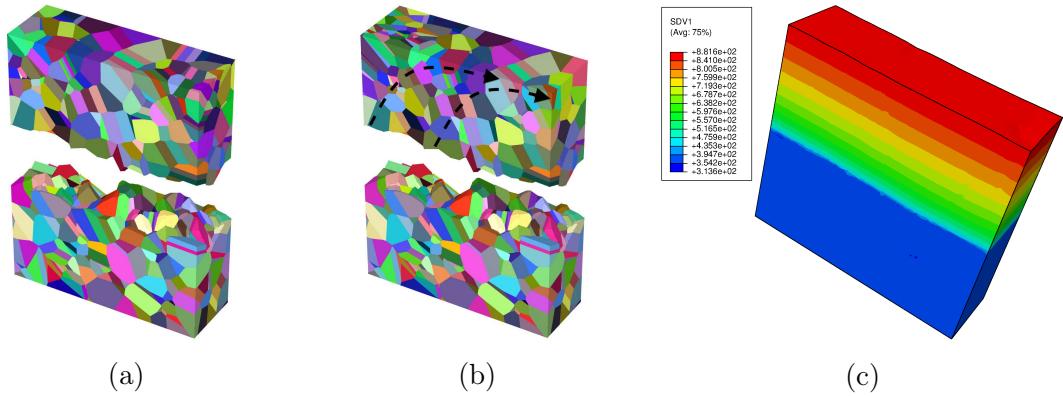


Figure 11: Isotropic lath morphology (a); Non isotropic morphology (b); Surface Hardening by introducing an increase of the resolved shear stress τ_0^s (c)

395 Moreover, the martensitic phase transformation requires particular crystallo-
 396 graphic relationship between the laths (BCC) and the matrix (Face-centered Cubic:
 397 FCC). In this study, the Kurdjumov-Sachs (KS) relationships are assumed since the
 398 X38CrMoV5-1 microstructure is similar to a low carbon steel [75, 76]. Considering
 399 the γ/α crystallographic planes relationship $\{111\}_\gamma || \{110\}_{\alpha'}$ and crystallographic
 400 orientation relationships $\langle 110 \rangle_\gamma || \langle 111 \rangle_{\alpha'}$, 24 variants are identified (see table
 401 A.9 in appendix). These variants are assigned to each PAG containing 4 packets
 402 where each packet contains 6 laths sharing the same habit. The 24 variants are
 403 randomly distributed (Fig. 12b). In such manner, global martensitic laths orienta-
 404 tions distribution is isotropic (Fig. 12c). For the layers close to the surface of the
 405 REV, the crystallographic texture given by KS relationships can be replaced by an
 406 experimental texture provided by EBSD measurements for a better consideration of
 407 the experimental evidence. The last effect to be considered deals with the surface
 408 roughness of the REV. Based on experimental results, the ultimate layer of RVE is
 409 differently meshed by a node coordinate displacement.

410

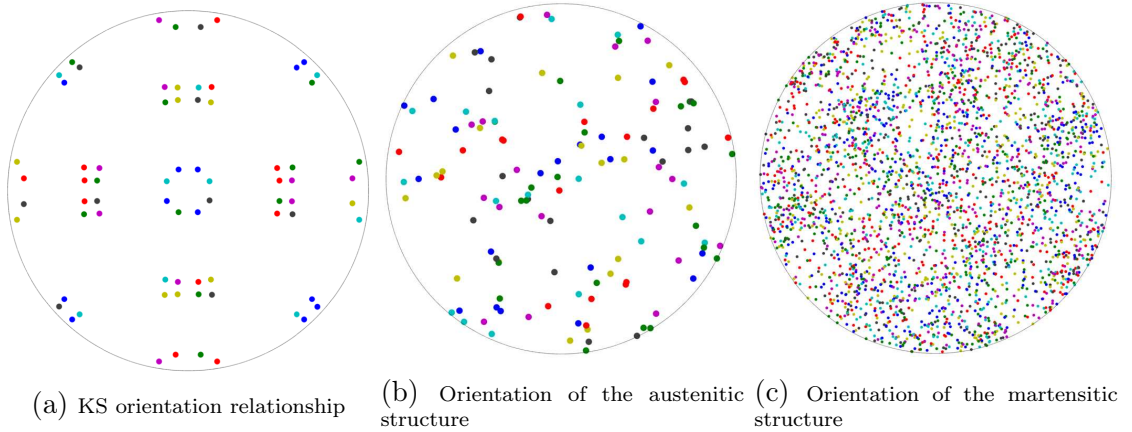


Figure 12: (100) pole figures (a) KS orientations relationship, (b) PAG, (c) martensitic lath

411 *4.4. Meshing and boundary conditions*

412 The FE meshing of Voronoï cells is not trivial. The meshing technique proposed
 413 by Quey [40] and implemented on Neper software is adopted. It includes an accurate
 414 discretization for taking into account the martensitic laths. This procedure needs
 415 some modifications in the morphology of the generated virtual microstructure. The
 416 edges of the Voronoï polyhedra with a short length ($l \leq l_c$, see Eq. 39) were
 417 eliminated. Therefore, some faces and vertexes of the Voronoï cells vanishes and the
 418 virtual microstructure is rebuilt by interpolation techniques as illustrated in Fig. 13.

$$l_c = 0.5r_cV_k^{\frac{1}{3}}; \quad r_c = 1.15 \quad (39)$$

419 where V_k is the volume of the Voronoï cell k and r_c a fixed parameter related to
 420 the mean size of the finite elements.

421

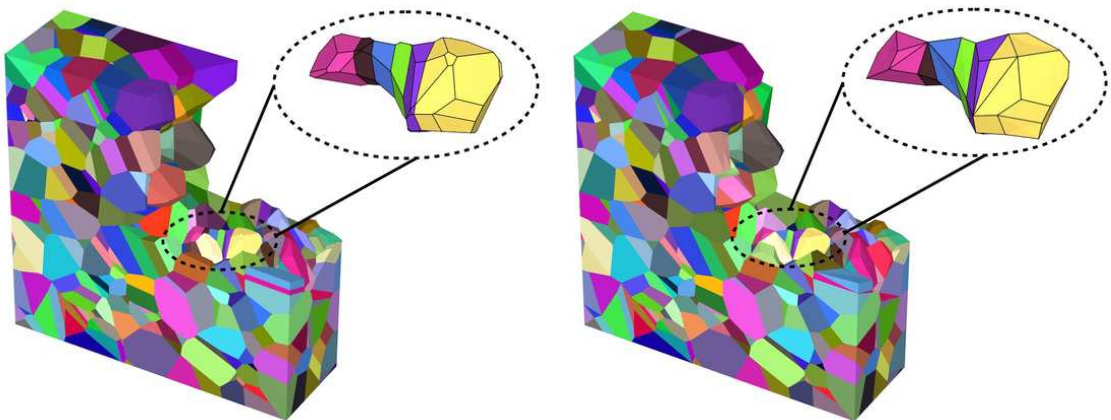


Figure 13: Improvement of the Voronoï cell shape for better mesh criteria

422 Then, a free meshing technique using quadratic tetrahedral elements with a full
 423 integration (namely $C3D10$ in ABAQUS software) is performed. 84177 elements are
 424 generated corresponding to an average value of 82 elements per cell which is relevant

425 for a multi-scale analysis [40]. The meshing analysis shows that the aspect ratio for
 426 only less than 0.59% of the finite elements is inadequate. The distribution of the
 427 elements per lath (e.g. Voronoï cell) is illustrated in Fig. 14a. The meshing and
 428 the boundary conditions prescribed on the RVE are shown in Fig. 14b. Two types
 429 of loading are considered, a tensile loading with a maximal strain of $\varepsilon = 8\%$ and a
 430 cyclic loading with $R_\varepsilon = \frac{\varepsilon_{min}}{\varepsilon_{max}} = 0.1$.

431

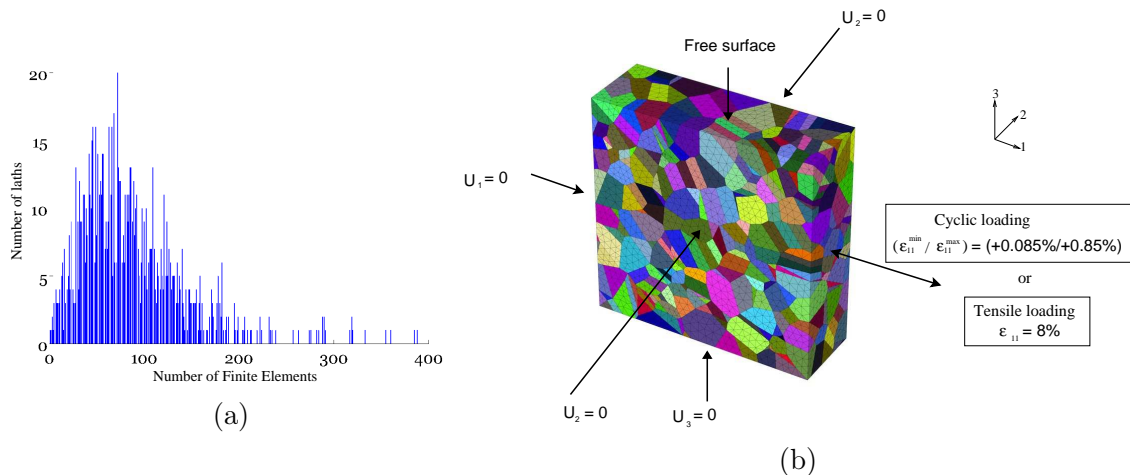


Figure 14: Distribution of the number of elements per lath (a); Meshing of the RVE and prescribed boundary conditions (b)

432 A FE parallel calculation is undertaken in ABAQUS software where the FETI
 433 (Finite Element Tearing and Interconnecting) method is used [77]. It allows the
 434 partition of the spatial domain into a set of disconnected sub-domains, each being
 435 assigned to an individual processor. In the present study, 8 processors with a clock
 436 rate of 2.8 GHz and a Random Access Memory of 30 GB per node are considered
 437 for each Finite Element calculation.

438 5. Results and discussions

439 5.1. Present and future issues of the approach

440 The knowledge of the actual mechanical loadings and the subsurface behavior of
 441 bodies in relative movement (sliding) requires the development of appropriate consti-
 442 tutive laws. In most cases, isotropic and macroscopic behavior is assumed. However,
 443 detailed investigations and microscopic observations on damage mechanisms reveal
 444 that the number of grains experiencing and bearing the shear strains at the extreme
 445 surfaces is limited [43, 54]. Therefore it becomes mandatory to distinguish the me-
 446 chanical behavior at the subsurface from the bulk. The grain boundaries emerging
 447 at surface, the interaction between surface and active dislocations in these grains,
 448 rupturing of well-orientated secondary phases (carbides, non spherical precipitates),
 449 rolling of spherical second phases or debris and specific crystallographic orientation
 450 of each grain cause various damage mechanisms. These mechanisms can simultane-
 451 ously be activated and even coupled, accelerating the processes and accumulation
 452 of damages. Under incremental shear straining the subsurface plastic yielding can

453 occur. The magnitude of the plastic yielding decreases inwards from the surface.
 454 One can observe that in addition to texturing of the martensitic laths and subse-
 455 quent PAGs beneath the surface of pins, micro-cavities (with different sizes) are also
 456 formed under excessive and cumulative shear straining (See Fig. 8 in [54]). At triple
 457 grains junction, the orientation of each laths packet and different crystallographic
 458 orientation of grains lead to micro-tearing and to the formation of micro-cavities
 459 as a consequence of the shear strain accumulations and an important stress/strain
 460 tri-axiality state. The micro-tearing located beneath the working surface can gener-
 461 ate wear debris. Under such complex conditions the macroscopic and isotropic
 462 constitutive laws might fail to well describe the subsurface behavior. Defining a
 463 *damage process zone* beneath the working surface of pins used in tribology investi-
 464 gations, Boher et al have proposed a wear model based on cumulative shear straining
 465 [78]. The fundamental of this model is inspired from Manson-Coffin law for LCF
 466 life prediction. The authors suppose that debris are emitted once the cumulative
 467 shear strain increment reaches the shear ductility. In this model, the plastic shear
 468 strain increment is evaluated by a macroscopic finite element simulation of a pin on
 469 a rotating disc. At this scale of investigation, the microstructure features drastically
 470 influence the behavior of the subsurface and cannot be neglected. Our approach
 471 can definitively improve the assessment of the cumulative shear strain increment
 472 required in the wear model [78].

473 The model results are reported hereafter under tensile and cyclic loading condi-
 474 tions for emphasizing the local behavior of individual lath, lath packets and PAGs.
 475 Many numerical results are extracted from the FE analysis for evaluating the stress
 476 and strain components at different scales such as:

- 477 • von Mises stress and inelastic strains,
- 478 • number of active slip systems,
- 479 • accumulated intrinsic dissipation Θ , i.e. the integral in time of Eq. 15.

480 Some of these results are compared with experimental tensile tests using DIC
 481 analysis.

482 5.2. Tensile loading

483 Several assumptions concerning the orientations relationships (KS or experimen-
 484 tal), the shape of the martensitic laths (anisotropic aspect), the shape of the surface
 485 (flat or rough) are examined (table 6).

486

Table 6: Tensile test conditions used for numerical simulations

Test condition	Crystallographic Orientations	Surface hardening	shape of the surface
1	KS	non	flat
2	KS	yes	flat
3	experimental	yes	flat
4	experimental	yes	rough

487 Fig. 15 illustrates the results (i.e. maps of the von Mises stress (a); the number
 488 of active slip systems (b); the intrinsic dissipation (c)) for a total deformation of
 489 8% and test condition 1. The von Mises stress shows significant stress concentra-
 490 tions close to the martensitic laths or PAG boundaries which are mainly influenced
 491 by the crystallographic orientations. The number of active slip systems does not
 492 show specific stress localization. The intrinsic dissipation reveals the zones where
 493 the inelastic strain is high. Unlike the macroscopic modeling of the behavior where
 494 the free surface of the specimen remains unchanged, one can notice that multi-scale
 495 crystal plasticity well predicts the free surface roughening.

496

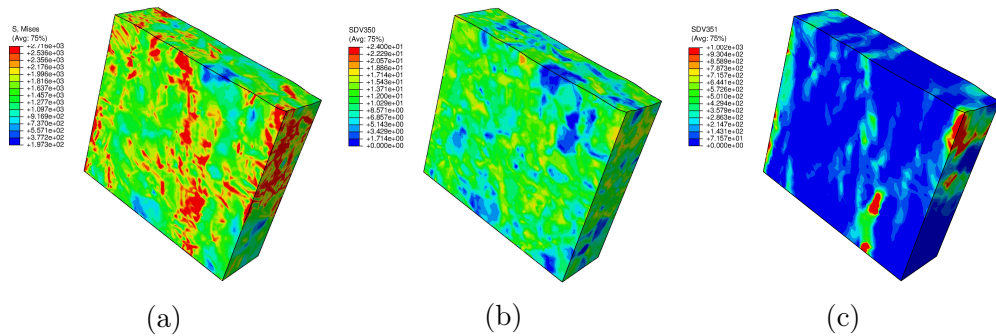


Figure 15: Equivalent von Mises stress component (a), number of active slip systems (b) and intrinsic dissipation (c) for the test conditions 1

497 Test conditions 2, 3 and 4 (table 6) are examined in order to be more realis-
 498 tic. Fig. 16a illustrates that the macroscopic strain-stress responses at the scale
 499 of the RVE are very close whatever test conditions. However, important variation
 500 in the local von Mises stress are found after 8% straining. The von Mises stress
 501 maps reveal that the stress concentrations are greatly influenced by the initial ori-
 502 entation relationships (Fig. 16b-16c). This effect is predominant within the upper
 503 half of the RVE where the crystallographic orientation relationships are identified
 504 by EBSD. Nevertheless, it should be mentioned that the lower half of the RVE is
 505 also affected by stress concentration while KS orientation relationships are identical
 506 for all simulated test conditions. When the rough surface is modeled (test condition
 507 4), the stress fields drastically change at the free surface while no such variation is
 508 observed for the other test conditions (2 and 3).

509

510 The stress-strain curves are numerically simulated for test condition 4 at differ-
 511 ent scales (scale of the RVE (a); of the PAG (b); of the lath packets (d) ; of the
 512 laths (d), Fig. 17) . First, one can notice that the stress-strain response obtained
 513 at the RVE scale is quite similar to the tensile experimental curve and also to the
 514 simulated stress-strain curve using the mean field scale transition rule (Fig. 8d).
 515 It means that the parameters identified using the β model and the FE method are
 516 consistent. The strain field heterogeneity increases when the scale decreases. In-
 517 deed, at the martensitic lath scale, a maximal strain level of 0.9 can be reached.
 518 The maximal stress can be 250% higher than the global macroscopic stresses (mea-
 519 sured or simulated). The number of the active slip systems strongly depends on the
 520 crystallographic orientation of a given lath and its morphology, this is why, when

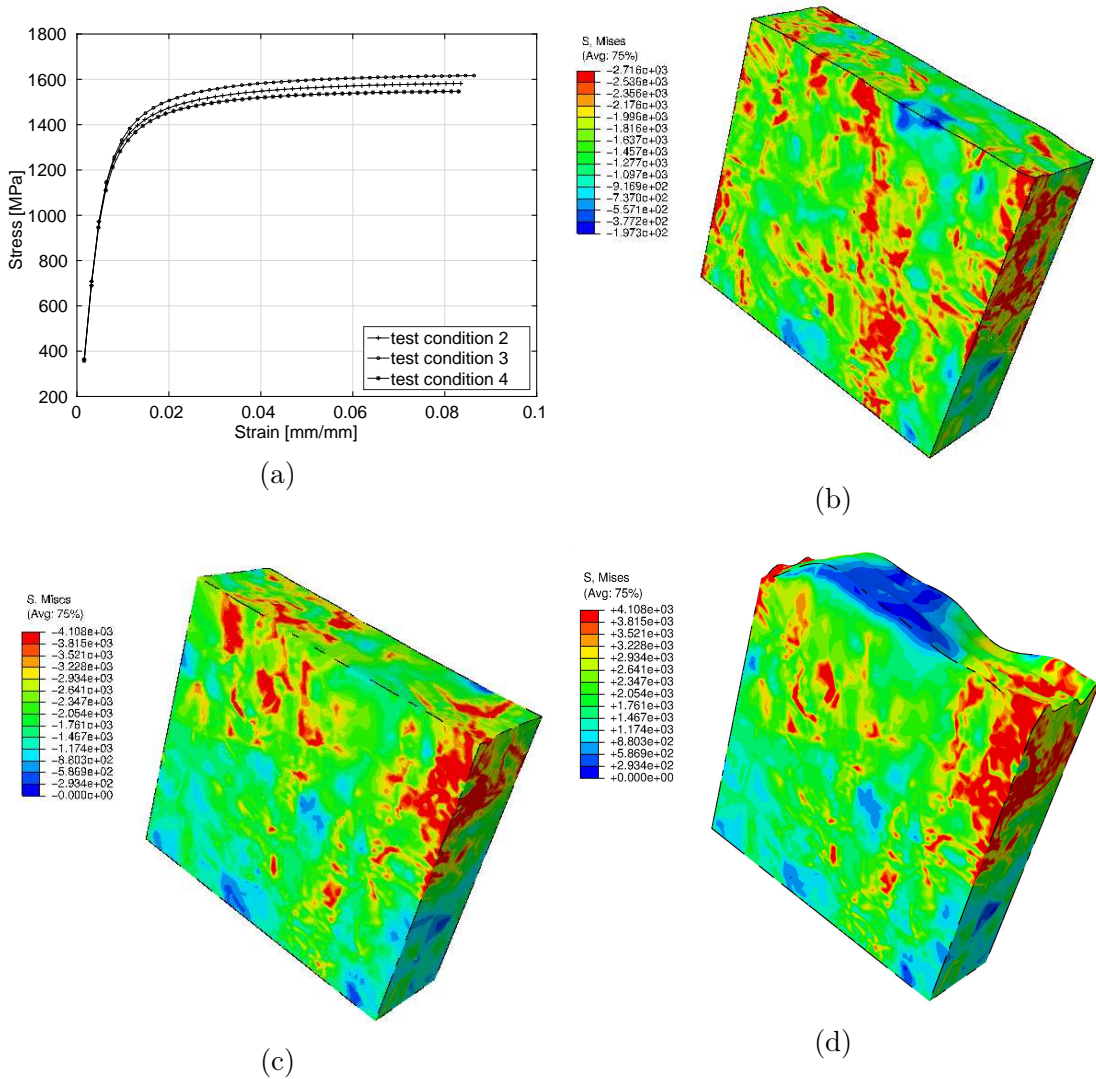


Figure 16: Macroscopic Strain-Stress response for test conditions 2 , 3 and 4 (a); von Mises stress field for the test conditions 2 (b); 3 (c) and 4 (d)

521 the simulated stresses for two laths may be very close, their local strains could be
522 very different. The comparison between the strain fields calculated by FE and mea-
523 sured by DIC is not trivial. It requires a high-performance digital image correlation
524 technique allowing a mapping of the strain fields at a microscopic scale [46]. In fact,
525 there is shortcoming to apply 2D strain field measurements on microstructure with
526 3D distribution of phases and precipitates. Also, the number of data collected (e.g.
527 strain field) from DIC measurements (2D) and RVE simulations (3D) are very dif-
528 ferent. Therefore, the number of data is collected for each major strain level. Then
529 the maximum value for the data collected, is extracted. At the end, a ratio of each
530 data collected over this maximum value is calculated. Through the normalization
531 method, experimental and simulated results can be compared as a function of major
532 strain levels (Fig. 18, for the test conditions 4 and a macroscopic major strain of 3%).
533

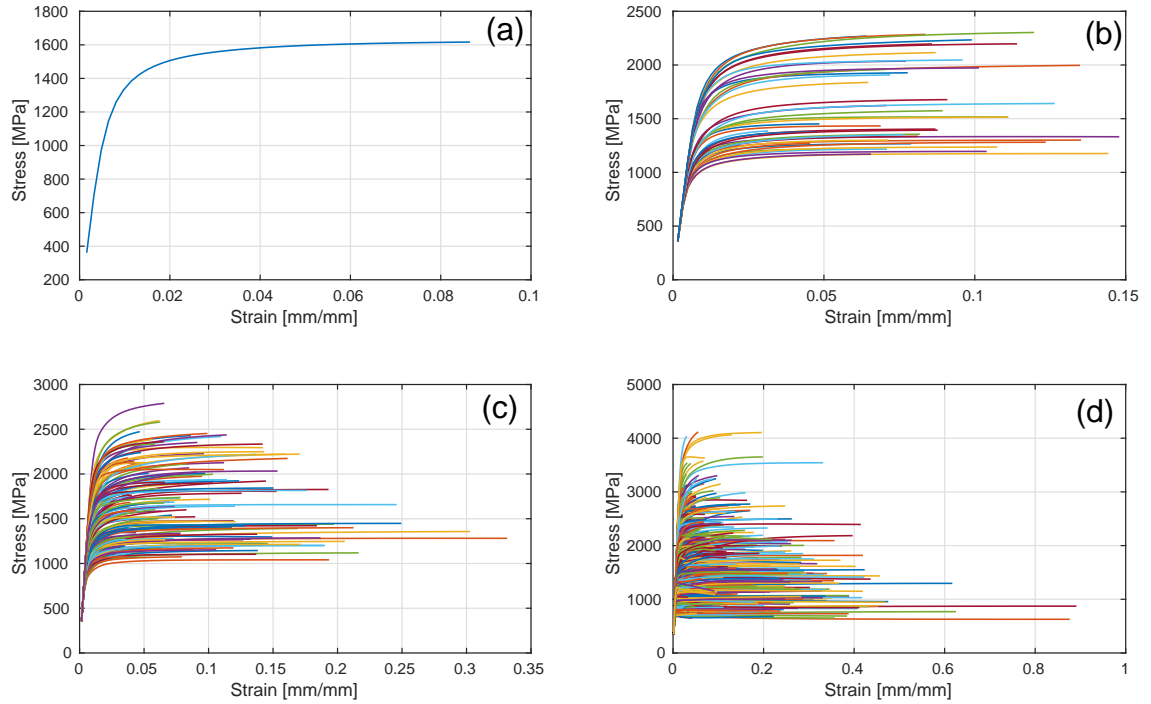


Figure 17: Strain-Stress curves under a tensile loading at different scales: (a) macroscopic, i.e. RVE behavior (well reproducing the experimental variation of the stress versus the strain in a tensile condition) ; (b) different PAG; (c) different lath packets; and (d) different martensitic laths (showing a huge scattering) using test conditions 4 (experimental crystallographic orientation provided by EBSD at the upper half of the RVE, considering a surface hardening through a decrease of the resolved shear stress and taking into account a roughness of the RVE surface). One can notice that the scattering in (b) and (c) are reduced in comparison with (d) due to the scale of the evaluations and tending towards the macroscopic curve (a).

534 5.3. Cyclic loading

535 9 cyclic tests (see Fig. 14b) are conducted on the RVE for different conditions
 536 (table 7). Similarly to the tensile tests, different assumptions can be made. A flat
 537 surface is considered. In one case, a microstructure is randomly generated by using
 538 the Kurdjumov and Sachs (KS) relationships with (test condition 6) or without (test
 539 condition 5) considering hardening of the surface on the upper half of the RVE as
 540 illustrated in Fig. 11c. In the second case, the measured crystallographic relation-
 541 ships by EBSD is used to generate this microstructure (test condition 7).

542

Table 7: Test conditions investigated in the numerical simulations for the cyclic tests

Test condition	Crystallographic Orientations	Surface hardening	shape of the surface
5	KS	non	flat
6	KS	yes	flat
7	experimental	yes	flat

543 Fig. 19a compares the average value of the stress-strain loops obtained by FE
 544 simulation at the RVE scale for the test conditions 5 to 7 and the cycles 1 and 9.
 545 This average value is in fact given by the extracted computed stress-strain values

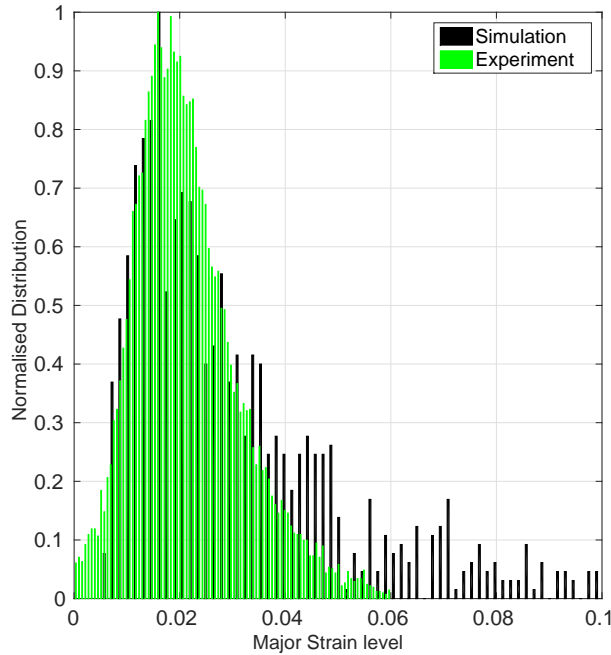


Figure 18: Distribution of the laths over the strain levels for an average strain level of 3%

546 at the level of laths, packets of laths and PAG. The trend for the test conditions 6
 547 and 7 are close even though the considered textures are different (KS relations and
 548 experimental by EBSD) whereas a significant change is observed in the stress level of
 549 test condition 5 for which no surface hardening is considered. Fig. 19b-19c gives the
 550 local von Mises stress at the maximal strain level of the cycle 9 for each test condi-
 551 tion. For the test conditions 5 and 6, the surface hardening introduced at the upper
 552 half of the RVE influences the stress distribution at the lower half even if the same
 553 crystallographic relations are considered. Moreover, a similar surface hardening is
 554 considered but with different crystallographic relations (test conditions 6 and 7), it
 555 is observed that the stress distribution is quite different inside the RVE while the
 556 RVE strain-stress response are similar (Fig. 19a). Fig. 20 shows the strain-stress
 557 responses for test condition 7 at different scales and for cycles 1 and 9. At the RVE
 558 scale, a plastic shakedown is observed between cycle 1 and 9 (Fig. 20 a-d). At the
 559 PAG scale, the plastic shakedown is not yet completed (Fig. 20 b-e). In fact, at the
 560 laths scale, the plastic ratcheting is very active, thus influencing the behavior at the
 561 PAG level. Fig. 20 c-f show clearly the enlarging of the stress-strain hysteresis loop.
 562

563 6. Conclusions

564 The surface modeling of tool steels are investigated at room temperature by
 565 experimental testing and numerical simulation. The elasto-viscoplastic equations
 566 are formulated at the scale of the slip systems considering an isotropic and kine-
 567 matic hardening variables to predict both tensile and cyclic loadings. Phenomeno-
 568 logical constitutive equations of Meric and Cailletaud [34, 35] are adapted for the

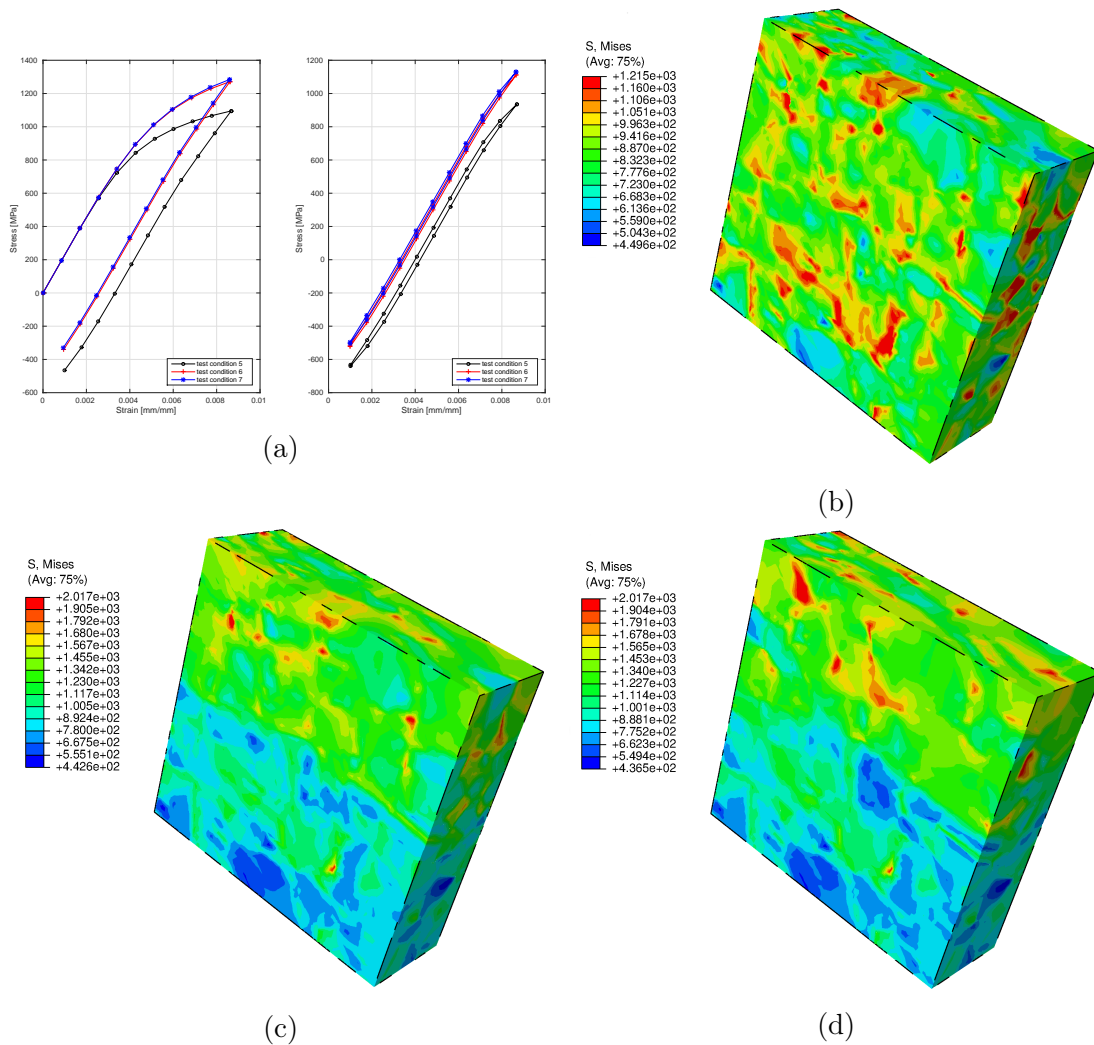


Figure 19: Macroscopic Strain-Stress response for test conditions 5 , 6 and 7 for the 1st (a) and the 9th (b) cycle; von Mises stress field for the test conditions 5 (b); 6 (c) and 7 (d) at the maximal strain of the 9th cycle

569 X38CrMoV5-1 double tempered martensitic steel with randomly oriented laths. The
 570 thermodynamic framework of the non reversible phenomena is respected at the lev-
 571 els of the slip systems, laths, packets of laths and PAG.

572

573 The following points can be addressed:

574 • DIC technique is used to propose a relevant RVE for this steel and also to
 575 determine the local strain fields.

576 • Two mean field approaches [18, 19] are applied for identifying the parameters
 577 of the constitutive laws. These methods ensure the transition between the slip
 578 systems and the RVE behavior.

579 • A full field approach using FE method takes into account explicitly the mi-
 580 crostructure features of the steel (martensitic laths, crystallographic orienta-
 581 tions, grain morphology). Voronoï tessellation is used to generate the virtual

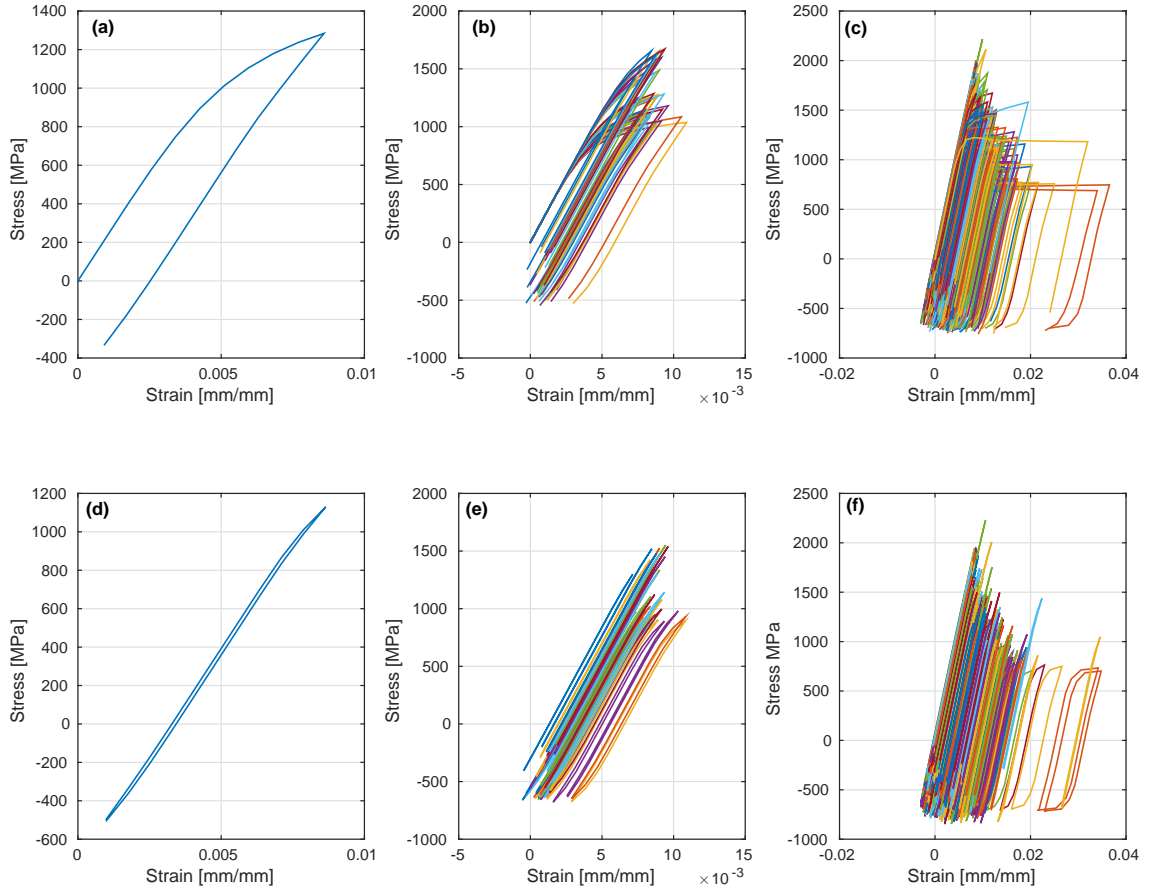


Figure 20: Strain-Stress curves under cyclic loading at the scale of the RVE (a,d), the PAG (b,e) and the martensitic laths (c,f) at the maximal strain of the 1st (a,b,c) and the 9th cycle (d,e,f) for the test conditions 7

582 microstructure [40]. This approach is based on a direct resolution scheme
 583 developed by Peirce [15, 16] and a predictor/corrector algorithm of Simo [70].

584 • The virtual microstructure is generated either based on EBSD measurements
 585 or Kurdjumov-Sachs crystallographic relationships between the matrix (FCC)
 586 and the laths (BCC). It is observed that the surface hardening of the layer
 587 of RVE influences the other half of the RVE behavior for different crystallo-
 588 graphic orientations. The effect of the surface aspects (plane or rough) is also
 589 investigated.

590 • The reliability of modeling approach is assessed for different loading conditions
 591 and microstructural aspects. An acceptable agreement between DIC measure-
 592 ments and the FE simulation is found for the local distribution of the strain
 593 fields (only under tensile loading condition).

594 • Cyclic loading simulations show that a plastic shakedown occurs at RVE level.
 595 At the PAG scale, the plastic shakedown is not totally achieved. At the laths
 596 scale, plastic ratcheting is very active. Enlargement of stress-strain loops are
 597 clearly observed. This enlargement is less at the level of the PAG.

598 **Acknowledgement**

599 The authors would like to gratefully acknowledge the scientific grouping CALMIP
600 for its support with regard to the FE calculations. Most of them were run on a
601 supercomputer which was made available to the researchers. The authors deeply ac-
602 knowledge Dr. Christine Boher from Mines-Albi & Institut Clément Ader, for many
603 valuable and fruitful discussions and exchanges on the wear subsurface behavior of
604 bodies in movement.

605 **Appendix A.**

606 *Appendix A.1. Interaction Matrix and Schmid-Boas and Miller notation systems*

$$\tilde{\mathbf{h}} = \begin{pmatrix} A1 & B1 & C1 & G1 & H1 & I1 & D2 & E2 & C2 & J2 & K2 & L2 & D3 & B3 & F3 & M3 & N3 & O3 & A4 & E4 & F4 & P4 & Q4 & R4 \\ A1 & h_8 & h_2 & h_2 & h_3 & h_3 & h_3 & h_4 & h_4 & h_4 & h_5 & h_5 & h_5 & h_4 & h_4 & h_4 & h_5 & h_5 & h_5 & h_4 & h_4 & h_4 & h_5 & h_5 & h_5 \\ B1 & h_2 & h_8 & h_2 & h_3 & h_3 & h_3 & h_4 & h_4 & h_4 & h_5 & h_5 & h_5 & h_4 & h_4 & h_4 & h_5 & h_5 & h_5 & h_4 & h_4 & h_4 & h_5 & h_5 & h_5 \\ C1 & h_2 & h_2 & h_8 & h_3 & h_3 & h_3 & h_4 & h_4 & h_4 & h_5 & h_5 & h_5 & h_4 & h_4 & h_4 & h_5 & h_5 & h_5 & h_4 & h_4 & h_4 & h_5 & h_5 & h_5 \\ G1 & h_3 & h_3 & h_3 & h_1 & h_6 & h_6 & h_5 & h_5 & h_5 & h_7 & h_7 & h_7 & h_5 & h_5 & h_5 & h_7 & h_7 & h_7 & h_5 & h_5 & h_5 & h_7 & h_7 & h_7 \\ H1 & h_3 & h_3 & h_3 & h_6 & h_1 & h_6 & h_5 & h_5 & h_5 & h_7 & h_7 & h_7 & h_5 & h_5 & h_5 & h_7 & h_7 & h_7 & h_5 & h_5 & h_5 & h_7 & h_7 & h_7 \\ I1 & h_3 & h_3 & h_3 & h_6 & h_6 & h_1 & h_5 & h_5 & h_5 & h_7 & h_7 & h_7 & h_5 & h_5 & h_5 & h_7 & h_7 & h_7 & h_5 & h_5 & h_5 & h_7 & h_7 & h_7 \\ D2 & h_4 & h_4 & h_4 & h_5 & h_5 & h_5 & h_8 & h_2 & h_2 & h_3 & h_3 & h_3 & h_4 & h_4 & h_4 & h_5 & h_5 & h_5 & h_4 & h_4 & h_4 & h_5 & h_5 & h_5 \\ E2 & h_4 & h_4 & h_4 & h_5 & h_5 & h_5 & h_2 & h_8 & h_2 & h_3 & h_3 & h_3 & h_4 & h_4 & h_4 & h_5 & h_5 & h_5 & h_4 & h_4 & h_4 & h_5 & h_5 & h_5 \\ C2 & h_4 & h_4 & h_4 & h_5 & h_5 & h_5 & h_2 & h_2 & h_8 & h_3 & h_3 & h_3 & h_4 & h_4 & h_4 & h_5 & h_5 & h_5 & h_4 & h_4 & h_4 & h_5 & h_5 & h_5 \\ J2 & h_5 & h_5 & h_5 & h_7 & h_7 & h_7 & h_3 & h_3 & h_3 & h_1 & h_6 & h_6 & h_5 & h_5 & h_5 & h_7 & h_7 & h_7 & h_5 & h_5 & h_5 & h_7 & h_7 & h_7 \\ K2 & h_5 & h_5 & h_5 & h_7 & h_7 & h_7 & h_3 & h_3 & h_3 & h_6 & h_1 & h_6 & h_5 & h_5 & h_5 & h_7 & h_7 & h_7 & h_5 & h_5 & h_5 & h_7 & h_7 & h_7 \\ L2 & h_5 & h_5 & h_5 & h_7 & h_7 & h_7 & h_3 & h_3 & h_3 & h_6 & h_6 & h_1 & h_5 & h_5 & h_5 & h_7 & h_7 & h_7 & h_5 & h_5 & h_5 & h_7 & h_7 & h_7 \\ D3 & h_4 & h_4 & h_4 & h_5 & h_5 & h_5 & h_4 & h_4 & h_4 & h_5 & h_5 & h_5 & h_8 & h_2 & h_2 & h_3 & h_3 & h_3 & h_4 & h_4 & h_4 & h_5 & h_5 & h_5 \\ B3 & h_4 & h_4 & h_4 & h_5 & h_5 & h_5 & h_4 & h_4 & h_4 & h_5 & h_5 & h_5 & h_2 & h_8 & h_2 & h_3 & h_3 & h_3 & h_4 & h_4 & h_4 & h_5 & h_5 & h_5 \\ F3 & h_4 & h_4 & h_4 & h_5 & h_5 & h_5 & h_4 & h_4 & h_4 & h_5 & h_5 & h_5 & h_2 & h_2 & h_8 & h_3 & h_3 & h_3 & h_4 & h_4 & h_4 & h_5 & h_5 & h_5 \\ M3 & h_5 & h_5 & h_5 & h_7 & h_7 & h_7 & h_5 & h_5 & h_5 & h_7 & h_7 & h_7 & h_3 & h_3 & h_3 & h_1 & h_6 & h_6 & h_5 & h_5 & h_5 & h_7 & h_7 & h_7 \\ N3 & h_5 & h_5 & h_5 & h_7 & h_7 & h_7 & h_5 & h_5 & h_5 & h_7 & h_7 & h_7 & h_3 & h_3 & h_3 & h_6 & h_1 & h_6 & h_5 & h_5 & h_5 & h_7 & h_7 & h_7 \\ O3 & h_5 & h_5 & h_5 & h_7 & h_7 & h_7 & h_5 & h_5 & h_5 & h_7 & h_7 & h_7 & h_3 & h_3 & h_3 & h_6 & h_6 & h_1 & h_5 & h_5 & h_5 & h_7 & h_7 & h_7 \\ A4 & h_4 & h_4 & h_4 & h_5 & h_5 & h_5 & h_4 & h_4 & h_4 & h_5 & h_5 & h_5 & h_4 & h_4 & h_4 & h_5 & h_5 & h_5 & h_8 & h_2 & h_2 & h_3 & h_3 & h_3 \\ E4 & h_4 & h_4 & h_4 & h_5 & h_5 & h_5 & h_4 & h_4 & h_4 & h_5 & h_5 & h_5 & h_4 & h_4 & h_4 & h_5 & h_5 & h_5 & h_2 & h_8 & h_2 & h_3 & h_3 & h_3 \\ F4 & h_4 & h_4 & h_4 & h_5 & h_5 & h_5 & h_4 & h_4 & h_4 & h_5 & h_5 & h_5 & h_4 & h_4 & h_4 & h_5 & h_5 & h_5 & h_2 & h_8 & h_2 & h_3 & h_3 & h_3 \\ P4 & h_5 & h_5 & h_5 & h_7 & h_7 & h_7 & h_5 & h_5 & h_5 & h_7 & h_7 & h_7 & h_5 & h_5 & h_5 & h_7 & h_7 & h_7 & h_3 & h_3 & h_3 & h_1 & h_6 & h_6 \\ Q4 & h_5 & h_5 & h_5 & h_7 & h_7 & h_7 & h_5 & h_5 & h_5 & h_7 & h_7 & h_7 & h_5 & h_5 & h_5 & h_7 & h_7 & h_7 & h_3 & h_3 & h_3 & h_6 & h_1 & h_6 \\ R4 & h_5 & h_5 & h_5 & h_7 & h_7 & h_7 & h_5 & h_5 & h_5 & h_7 & h_7 & h_7 & h_5 & h_5 & h_5 & h_7 & h_7 & h_7 & h_3 & h_3 & h_3 & h_6 & h_6 & h_1 \end{pmatrix} \quad (\text{A.1})$$

Table A.8: Normalized Schmid-Boas and Miller notation systems

Schmid-Boas	A1	B1	C1	G1	H1	I1	D2	E2	C2	J2	K2	L2
Slip plane \underline{l}^s	$\frac{(\bar{1}\bar{1}0)}{\sqrt{2}}$	$\frac{(\bar{1}0\bar{1})}{\sqrt{2}}$	$\frac{(0\bar{1}\bar{1})}{\sqrt{2}}$	$\frac{(\bar{1}\bar{1}\bar{2})}{\sqrt{6}}$	$\frac{(\bar{1}2\bar{1})}{\sqrt{6}}$	$\frac{(\bar{2}\bar{1}\bar{1})}{\sqrt{6}}$	$\frac{(\bar{1}\bar{1}0)}{\sqrt{2}}$	$\frac{(\bar{1}0\bar{1})}{\sqrt{2}}$	$\frac{(0\bar{1}\bar{1})}{\sqrt{2}}$	$\frac{(\bar{1}\bar{1}\bar{2})}{\sqrt{6}}$	$\frac{(\bar{1}2\bar{1})}{\sqrt{6}}$	$\frac{(\bar{2}\bar{1}\bar{1})}{\sqrt{6}}$
Slip direction \underline{n}^s	$\frac{[\bar{1}\bar{1}\bar{1}]}{\sqrt{3}}$	$\frac{[\bar{1}\bar{1}\bar{1}]}{\sqrt{3}}$	$\frac{[\bar{1}\bar{1}\bar{1}]}{\sqrt{3}}$	$\frac{[\bar{1}\bar{1}\bar{1}]}{\sqrt{3}}$	$\frac{[\bar{1}\bar{1}\bar{1}]}{\sqrt{3}}$	$\frac{[\bar{1}\bar{1}\bar{1}]}{\sqrt{3}}$	$\frac{[\bar{1}\bar{1}\bar{1}]}{\sqrt{3}}$	$\frac{[\bar{1}\bar{1}\bar{1}]}{\sqrt{3}}$	$\frac{[\bar{1}\bar{1}\bar{1}]}{\sqrt{3}}$	$\frac{[\bar{1}\bar{1}\bar{1}]}{\sqrt{3}}$	$\frac{[\bar{1}\bar{1}\bar{1}]}{\sqrt{3}}$	$\frac{[\bar{1}\bar{1}\bar{1}]}{\sqrt{3}}$
Schmid-Boas	D3	B3	F3	M3	N3	O3	A4	E4	F4	P4	Q4	R4
Slip plane \underline{l}^s	$\frac{(\bar{1}\bar{1}0)}{\sqrt{2}}$	$\frac{(\bar{1}0\bar{1})}{\sqrt{2}}$	$\frac{(0\bar{1}\bar{1})}{\sqrt{2}}$	$\frac{(\bar{1}\bar{1}\bar{2})}{\sqrt{6}}$	$\frac{(\bar{1}\bar{1}\bar{2})}{\sqrt{6}}$	$\frac{(\bar{2}\bar{1}\bar{1})}{\sqrt{6}}$	$\frac{(\bar{1}\bar{1}0)}{\sqrt{2}}$	$\frac{(\bar{1}0\bar{1})}{\sqrt{2}}$	$\frac{(0\bar{1}\bar{1})}{\sqrt{2}}$	$\frac{(\bar{1}\bar{1}\bar{2})}{\sqrt{6}}$	$\frac{(\bar{1}2\bar{1})}{\sqrt{6}}$	$\frac{(\bar{2}\bar{1}\bar{1})}{\sqrt{6}}$
Slip direction \underline{n}^s	$\frac{[\bar{1}\bar{1}\bar{1}]}{\sqrt{3}}$	$\frac{[\bar{1}\bar{1}\bar{1}]}{\sqrt{3}}$	$\frac{[\bar{1}\bar{1}\bar{1}]}{\sqrt{3}}$	$\frac{[\bar{1}\bar{1}\bar{1}]}{\sqrt{3}}$	$\frac{[\bar{1}\bar{1}\bar{1}]}{\sqrt{3}}$	$\frac{[\bar{1}\bar{1}\bar{1}]}{\sqrt{3}}$	$\frac{[\bar{1}\bar{1}\bar{1}]}{\sqrt{3}}$	$\frac{[\bar{1}\bar{1}\bar{1}]}{\sqrt{3}}$	$\frac{[\bar{1}\bar{1}\bar{1}]}{\sqrt{3}}$	$\frac{[\bar{1}\bar{1}\bar{1}]}{\sqrt{3}}$	$\frac{[\bar{1}\bar{1}\bar{1}]}{\sqrt{3}}$	$\frac{[\bar{1}\bar{1}\bar{1}]}{\sqrt{3}}$

607 *Appendix A.2. Variant orientation of a PAG according to the KS relationship*

608 In the present investigation, 24 laths and 4 blocks (6 laths per block) are included
 609 in each PAG. The KS relationship assumes that a block is defined by a parallelism
 610 relationship between two crystallographic planes given by the α' (martensitic lath)
 611 and γ (austenitic grain) phases. The parallelism relationship for the variant orien-
 612 tations between two crystallographic directions is recalled in Table A.9.

Table A.9: Variant orientation of a PAG according to the KS relationship

Block	Parallelism	Variant	Parallelism
1	$(111)_\gamma \parallel (011)_{\alpha'}$	1	$[\bar{1}01]_\gamma \parallel [\bar{1}\bar{1}1]_{\alpha'}$
		2	$[\bar{1}01]_\gamma \parallel [\bar{1}1\bar{1}]_{\alpha'}$
		3	$[0\bar{1}1]_\gamma \parallel [\bar{1}\bar{1}1]_{\alpha'}$
		4	$[0\bar{1}1]_\gamma \parallel [\bar{1}1\bar{1}]_{\alpha'}$
		5	$[1\bar{1}0]_\gamma \parallel [\bar{1}\bar{1}1]_{\alpha'}$
		6	$[1\bar{1}0]_\gamma \parallel [\bar{1}1\bar{1}]_{\alpha'}$
2	$(1\bar{1}1)_\gamma \parallel (011)_{\alpha'}$	7	$[10\bar{1}]_\gamma \parallel [\bar{1}\bar{1}1]_{\alpha'}$
		8	$[10\bar{1}]_\gamma \parallel [\bar{1}1\bar{1}]_{\alpha'}$
		9	$[\bar{1}\bar{1}0]_\gamma \parallel [\bar{1}\bar{1}1]_{\alpha'}$
		10	$[\bar{1}\bar{1}0]_\gamma \parallel [\bar{1}1\bar{1}]_{\alpha'}$
		11	$[011]_\gamma \parallel [\bar{1}\bar{1}1]_{\alpha'}$
		12	$[011]_\gamma \parallel [\bar{1}1\bar{1}]_{\alpha'}$
3	$(\bar{1}11)_\gamma \parallel (011)_{\alpha'}$	13	$[0\bar{1}1]_\gamma \parallel [\bar{1}\bar{1}1]_{\alpha'}$
		14	$[0\bar{1}1]_\gamma \parallel [\bar{1}1\bar{1}]_{\alpha'}$
		15	$[\bar{1}0\bar{1}]_\gamma \parallel [\bar{1}\bar{1}1]_{\alpha'}$
		16	$[\bar{1}0\bar{1}]_\gamma \parallel [\bar{1}1\bar{1}]_{\alpha'}$
		17	$[110]_\gamma \parallel [\bar{1}\bar{1}1]_{\alpha'}$
		18	$[110]_\gamma \parallel [\bar{1}1\bar{1}]_{\alpha'}$
4	$(11\bar{1})_\gamma \parallel (011)_{\alpha'}$	19	$[\bar{1}10]_\gamma \parallel [\bar{1}\bar{1}1]_{\alpha'}$
		20	$[\bar{1}10]_\gamma \parallel [\bar{1}1\bar{1}]_{\alpha'}$
		21	$[0\bar{1}\bar{1}]_\gamma \parallel [\bar{1}\bar{1}1]_{\alpha'}$
		22	$[0\bar{1}\bar{1}]_\gamma \parallel [\bar{1}1\bar{1}]_{\alpha'}$
		23	$[101]_\gamma \parallel [\bar{1}\bar{1}1]_{\alpha'}$
		24	$[101]_\gamma \parallel [\bar{1}1\bar{1}]_{\alpha'}$

613 **References**

- 614 [1] B. J. Golden, D.-F. Li, Y. Guo, P. Tiernan, S. B. Leen, N. P. O’Dowd, Mi-
615 croscale deformation of a tempered martensite ferritic steel: Modelling and ex-
616 perimental study of grain and sub-grain interactions, *Journal of the Mechanics*
617 *and Physics of Solids* 86 (2016) 42 – 52.
- 618 [2] J. Dunlop, Y. M. Bréchet, L. Legras, Y. Estrin, Dislocation density-based mod-
619 elling of plastic deformation of zircaloy-4, *Materials Science and Engineering:*
620 *A* 443 (1 - 2) (2007) 77 – 86.
- 621 [3] Y. Li, V. Aubin, C. Rey, P. Bompard, Polycrystalline numerical simulation of
622 variable amplitude loading effects on cyclic plasticity and microcrack initiation
623 in austenitic steel 304L, *International Journal of Fatigue* 42 (2012) 71 – 81.
- 624 [4] A. L. Pécheur, F. Curtit, M. Clavel, J. Stephan, C. Rey, P. Bompard, Poly-
625 crystal modelling of fatigue: Pre-hardening and surface roughness effects on
626 damage initiation for 304L stainless steel, *International Journal of Fatigue* 45
627 (2012) 48 – 60.
- 628 [5] C. Frederick, P. Armstrong, A mathematical representation of the multiaxial
629 bauschinger effect, *Materials at High Temperatures* 24 (1) (2007) 1 – 26.
- 630 [6] J. Lemaitre, J.-L. Chaboche, *Mechanics of solid materials*, Cambridge Univer-
631 sity Press, 1994.
- 632 [7] L. Tabourot, M. Fivel, E. Rauch, Generalised constitutive laws for f.c.c. single
633 crystals, *Materials Science and Engineering: A* 234-236 (1997) 639 – 642.
- 634 [8] P. Franciosi, The concepts of latent hardening and strain hardening in metallic
635 single crystals, *Acta Metallurgica* 33 (9) (1985) 1601 – 1612.
- 636 [9] M. Lee, H. Lim, B. Adams, J. Hirth, R. Wagoner, A dislocation density-based
637 single crystal constitutive equation, *International Journal of Plasticity* 26 (7)
638 (2010) 925 – 938.
- 639 [10] B. Fournier, M. Sauzay, A. Pineau, Micromechanical model of the high tem-
640 perature cyclic behavior of 9-12% Cr martensitic steels, *International Journal*
641 *of Plasticity* 27 (11) (2011) 1803 – 1816.
- 642 [11] M. Sauzay, H. Brillet, I. Monnet, M. Mottot, F. Barcelo, B. Fournier, A. Pineau,
643 Cyclically induced softening due to low-angle boundary annihilation in a
644 martensitic steel, *Materials Science and Engineering: A* 400-401 (2005) 241
645 – 244.
- 646 [12] J. Hutchinson, Bounds and self-consistent estimates for creep of polycrystalline
647 materials, *Proceedings of the Royal Society of London A: Mathematical, Phys-*
648 *ical and Engineering Sciences* 348 (1652) (1976) 101 – 127.
- 649 [13] R. Asaro, Crystal plasticity, *Journal of Applied Mechanics* 50 (4b) (1983) 921
650 – 934.

- 651 [14] R. Asaro, Micromechanics of crystals and polycrystals, in: J. W. H. a. T. Y.
652 Wu (Ed.), *Advances in Applied Mechanics*, Vol. 23, Elsevier, 1983, pp. 1 – 115.
- 653 [15] D. Peirce, R. Asaro, A. Needleman, An analysis of nonuniform and localized
654 deformation in ductile single crystals, *Acta Metallurgica* 30 (6) (1982) 1087 –
655 1119.
- 656 [16] D. Peirce, R. Asaro, A. Needleman, Material rate dependence and localized
657 deformation in crystalline solids, *Acta Metallurgica* 31 (12) (1983) 1951 – 1976.
- 658 [17] B. Xu, Y. Jiang, A cyclic plasticity model for single crystals, *International*
659 *Journal of Plasticity* 20 (12) (2004) 2161 – 2178.
- 660 [18] M. Berveiller, A. Zaoui, An extension of the self-consistent scheme to plastically-
661 flowing polycrystals, *Journal of the Mechanics and Physics of Solids* 26 (5-6)
662 (1978) 325 – 344.
- 663 [19] G. Cailletaud, P. Pilvin, Utilisation de modèles polycristallins pour le calcul
664 par éléments finis, *Revue Européenne des Eléments* 3 (4) (1994) 515 – 541.
- 665 [20] F. Roters, P. Eisenlohr, L. Hantcherli, D. D. Tjahjanto, T. R. Bieler, D. Raabe,
666 Overview of constitutive laws, kinematics, homogenization and multiscale meth-
667 ods in crystal plasticity finite-element modeling: Theory, experiments, applica-
668 tions, *Acta Materialia* 58 (4) (2010) 1152 – 1211.
- 669 [21] D. McDowell, Viscoplasticity of heterogeneous metallic materials, *Materials Sci-*
670 *ence and Engineering: R: Reports* 62 (3) (2008) 67 – 123.
- 671 [22] D. McDowell, A perspective on trends in multiscale plasticity, *International*
672 *Journal of Plasticity* 26 (9) (2010) 1280 – 1309.
- 673 [23] J. Besson, G. Cailletaud, J.-L. Chaboche, S. Forest, M. Blétry, Non-linear me-
674 chanics of materials, Vol. 167 of *Solid Mechanics and Its Applications*, Springer,
675 2009.
- 676 [24] G. Cailletaud, S. Forest, D. Jeulin, F. Feyel, I. Galliet, V. Mounoury, S. Leroy,
677 Some elements of microstructural mechanics, *Computational Materials Science*
678 27 (3) (2003) 351 – 374.
- 679 [25] S. Forest, *Milieux continus généralisés et matériaux hétérogènes*, Presses de
680 l’Ecole des Mines, 2006.
- 681 [26] O. Diard, S. Leclercq, G. Rousselier, G. Cailletaud, Evaluation of finite element
682 based analysis of 3d multicrystalline aggregates plasticity: Application to crys-
683 tal plasticity model identification and the study of stress and strain fields near
684 grain boundaries, *International Journal of Plasticity* 21 (4) (2005) 691 – 722.
- 685 [27] E. Héripéré, M. Dexet, J. Crépin, L. Gélébart, A. Roos, M. Bornert, D. Calde-
686 maison, Coupling between experimental measurements and polycrystal finite
687 element calculations for micromechanical study of metallic materials, *Interna-*
688 *tional Journal of Plasticity* 23 (9) (2007) 1512 – 1539.

- 689 [28] Y. Guilhem, S. Basseville, F. Curtit, J.-M. Stéphan, G. Cailletaud, Numerical investigations of the free surface effect in three-dimensional polycrystalline
690 aggregates, *Computational Materials Science* 70 (2013) 150 – 162.
691
- 692 [29] A. Guery, F. Hild, F. Latourte, S. Roux, Slip activities in polycrystals deter-
693 mined by coupling dic measurements with crystal plasticity calculations, *Inter-
694 national Journal of Plasticity* 81 (2016) 249 – 266.
- 695 [30] C. Efstathiou, H. Sehitoglu, J. Lambros, Multiscale strain measurements of plas-
696 tically deforming polycrystalline titanium: Role of deformation heterogeneities,
697 *International Journal of Plasticity* 26 (1) (2010) 93 – 106.
- 698 [31] H. Lim, J. D. Carroll, C. C. Battaile, B. L. Boyce, C. R. Weinberger, Quanti-
699 tative comparison between experimental measurements and cp-fem predictions
700 of plastic deformation in a tantalum oligocrystal, *International Journal of Me-
701 chanical Sciences* 92 (2015) 98 – 108.
- 702 [32] C. Gérard, G. Cailletaud, B. Bacroix, Modeling of latent hardening produced
703 by complex loading paths in fcc alloys, *International Journal of Plasticity* 42
704 (2013) 194 – 212.
- 705 [33] G. Cailletaud, A micromechanical approach to inelastic behaviour of metals,
706 *International Journal of Plasticity* 8 (1) (1992) 55 – 73.
- 707 [34] L. Méric, , P. Poubanne, G. Cailletaud, Single crystal modeling for structural
708 calculations: Part 1-model presentation, *Journal of Engineering Materials and
709 Technology* 113 (1) (1991) 162 – 170.
- 710 [35] L. Méric, G. Cailletaud, Single crystal modeling for structural calculations:
711 Part 2-finite element implementation, *Journal of Engineering Materials and
712 Technology* 113 (1) (1991) 171 – 182.
- 713 [36] A. Zouaghi, Modélisation multi-échelle du comportement non linéaire et
714 hétérogène en surface de l'acier AISI H11, Thèse de doctorat, Université de
715 Toulouse (2015).
- 716 [37] A. Zouaghi, V. Velay, A. Soveja, F. Rezai-Aria, A Numerical Investigation
717 on the heterogeneous and anisotropic mechanical behaviour of AISI H11 steel
718 using various stress-strain formulations: a multi-scale approach, in: 11th World
719 Congress on Computational Mechanics, 2014, pp. 3415–3425.
- 720 [38] A. Alankar, D. P. Field, D. Raabe, Plastic anisotropy of electro-deposited pure
721 α -iron with sharp crystallographic $\langle 1\ 1\ 1 \rangle$ // texture in normal direction:
722 Analysis by an explicitly dislocation-based crystal plasticity model, *Internation-
723 al Journal of Plasticity* 52 (2014) 18 – 32.
- 724 [39] D. Cereceda, M. Diehl, F. Roters, D. Raabe, J. M. Perlado, J. Marian, Unravel-
725 ing the temperature dependence of the yield strength in single-crystal tungsten
726 using atomistically-informed crystal plasticity calculations, *International Jour-
727 nal of Plasticity* 78 (2016) 242 – 265.

- 728 [40] R. Quey, P. R. Dawson, F. Barbe, Large-scale 3D random polycrystals for the
729 finite element method: Generation, meshing and remeshing, *Computer Methods*
730 *in Applied Mechanics and Engineering* 200 (17-20) (2011) 1729 – 1745.
- 731 [41] C. Zhang, H. Li, P. Eisenlohr, W. Liu, C. Boehlert, M. Crimp, T. Bieler, Ef-
732 fect of realistic 3d microstructure in crystal plasticity finite element analysis of
733 polycrystalline ti-5al-2.5sn, *International Journal of Plasticity* 69 (2015) 21 –
734 35.
- 735 [42] D.-F. Li, B. J. Golden, N. P. O’Dowd, Multiscale modelling of mechanical
736 response in a martensitic steel: A micromechanical and length-scale-dependent
737 framework for precipitate hardening, *Acta Materialia* 80 (2014) 445 – 456.
- 738 [43] D. Raabe, M. Sachtler, H. Weiland, G. Scheele, Z. Zhao, Grain-scale mi-
739 cromechanics of polycrystal surfaces during plastic straining, *Acta Materialia*
740 51 (6) (2003) 1539 – 1560.
- 741 [44] Z. Zhao, M. Ramesh, D. Raabe, A. Cuitiño, R. Radovitzky, Investigation of
742 three-dimensional aspects of grain-scale plastic surface deformation of an alu-
743 minium oligocrystal, *International Journal of Plasticity* 24 (12) (2008) 2278 –
744 2297.
- 745 [45] C. Tasan, J. Hoefnagels, M. Diehl, D. Yan, F. Roters, D. Raabe, Strain local-
746 ization and damage in dual phase steels investigated by coupled in-situ defor-
747 mation experiments and crystal plasticity simulations, *International Journal of*
748 *Plasticity* 63 (2014) 198 – 210.
- 749 [46] C. Tasan, M. Diehl, D. Yan, C. Zambaldi, P. Shanthraj, F. Roters, D. Raabe,
750 Integrated experimental-simulation analysis of stress and strain partitioning in
751 multiphase alloys, *Acta Materialia* 81 (2014) 386 – 400.
- 752 [47] S. Morito, Y. Adachi, T. Ohba, Morphology and crystallography of sub-blocks
753 in ultra-low carbon lath martensite steel, *Materials Transactions* 50 (8) (2009)
754 1919 – 1923.
- 755 [48] H. Beladi, G. Rohrer, A. Rollett, V. Tari, P. Hodgson, The distribution of
756 intervariant crystallographic planes in a lath martensite using five macroscopic
757 parameters, *Acta Materialia* 63 (2014) 86 – 98.
- 758 [49] N. Mebarki, D. Delagnes, P. Lamesle, F. Delmas, C. Levaillant, Relationship
759 between microstructure and mechanical properties of a 5% Cr tempered marten-
760 sitic tool steel, *Materials Science and Engineering: A* 387 - 389 (15) (2004) 171
761 – 175.
- 762 [50] V. Velay, G. Bernhart, D. Delagnes, L. Penazzi, A continuum damage model
763 applied to high-temperature fatigue lifetime prediction of a martensitic tool
764 steel, *Fatigue and Fracture of Engineering Materials and Structures* 28 (11)
765 (2005) 1009–1023.

- 766 [51] F. Krumphals, B. Reggiani, L. Donati, T. Wlanis, C. Sommitsch, Deformation
767 behaviour of a ferritic hot-work tool steel with respect to the microstructure,
768 Computational Materials Science 52 (1) (2012) 40 – 45.
- 769 [52] M. Poitrimolt, M. Cheikh, G. Bernhart, V. Velay, Characterisation of the trans-
770 verse mechanical properties of carbon/carbon composites by spherical indenta-
771 tion, Carbon 66 (2014) 234 – 245.
- 772 [53] R. Moulart, R. Rotinat, F. Pierron, Full-field evaluation of the onset of mi-
773 croplasticity in a steel specimen, Mechanics of Materials 41 (11) (2009) 1207 –
774 1222.
- 775 [54] O. Barrau, C. Boher, R. Gras, F. Rézai-Aria, Analysis of the friction and wear
776 behaviour of hot work tool steel for forging, Wear 255 (7-12) (2003) 1444 –
777 1454.
- 778 [55] C. Zambaldi, C. Zehnder, D. Raabe, Orientation dependent deformation by slip
779 and twinning in magnesium during single crystal indentation, Acta Materialia
780 91 (2015) 267 – 288.
- 781 [56] T. Bieler, P. Eisenlohr, F. Roters, D. Kumar, D. Mason, M. Crimp, D. Raabe,
782 The role of heterogeneous deformation on damage nucleation at grain bound-
783 aries in single phase metals, International Journal of Plasticity 25 (9) (2009)
784 1655 – 1683.
- 785 [57] C. Hamelin, B. Diak, A. Pilkey, Multiscale modelling of the induced plastic
786 anisotropy in bcc metals, International Journal of Plasticity 27 (8) (2011) 1185
787 – 1202.
- 788 [58] A. Zeghadi, S. Forest, A.-F. Gourgues, O. Bouaziz, Ensemble averaging stress-
789 strain fields in polycrystalline aggregates with a constrained surface microstruc-
790 ture - Part 2: crystal plasticity, Philosophical Magazine 87 (8-9) (2007) 1425 –
791 1446.
- 792 [59] T. Hoc, S. Forest, Polycrystal modelling of IF-ti steel under complex loading
793 path, International Journal of Plasticity 17 (1) (2001) 65 – 85.
- 794 [60] A. Hlilou, I. B. Naceur, K. Saï, C. Gérard, S. Forest, G. Cailletaud, Generaliza-
795 tion of the polycrystalline β -model: Finite element assessment and application
796 to softening material behavior, Computational Materials Science 45 (4) (2009)
797 1104 – 1112.
- 798 [61] V. Velay, G. Bernhart, L. Penazzi, Cyclic behavior modeling of a tempered
799 martensitic hot work tool steel, International Journal of Plasticity 22 (3) (2006)
800 459–496.
- 801 [62] Z. Zhang, D. Delagnes, G. Bernhart, Anisothermal cyclic plasticity modelling
802 of martensitic steels, International Journal of Fatigue 24 (6) (2002) 635–648.

- 803 [63] R. Foerch, J. Besson, G. Cailletaud, P. Pilvin, Polymorphic constitutive equa-
804 tions in finite element codes, *Computer Methods in Applied Mechanics and*
805 *Engineering* 141 (3-4) (1997) 355 – 372.
- 806 [64] T. Erinosh, A. Cocks, F. Dunne, Texture, hardening and non-proportionality
807 of strain in bcc polycrystal deformation, *International Journal of Plasticity* 50
808 (2013) 170 – 192.
- 809 [65] S. Kuchnicki, A. Cuitiño, R. Radovitzky, Efficient and robust constitutive inte-
810 grators for single-crystal plasticity modeling, *International Journal of Plasticity*
811 22 (10) (2006) 1988 – 2011.
- 812 [66] S. Kuchnicki, R. Radovitzky, A. Cuitiño, An explicit formulation for multiscale
813 modeling of bcc metals, *International Journal of Plasticity* 24 (12) (2008) 2173
814 – 2191.
- 815 [67] H. Li, H. Yang, Z. Sun, A robust integration algorithm for implementing rate
816 dependent crystal plasticity into explicit finite element method, *International*
817 *Journal of Plasticity* 24 (2) (2008) 267 – 288.
- 818 [68] J. Rossiter, A. Brahme, M. Simha, K. Inal, R. Mishra, A new crystal plas-
819 ticity scheme for explicit time integration codes to simulate deformation in 3d
820 microstructures: Effects of strain path, strain rate and thermal softening on
821 localized deformation in the aluminum alloy 5754 during simple shear, *Internat-*
822 *ional Journal of Plasticity* 26 (12) (2010) 1702 – 1725.
- 823 [69] J. Segurado, R. A. Lebensohn, J. LLorca, C. Tomé, Multiscale modeling of
824 plasticity based on embedding the viscoplastic self-consistent formulation in
825 implicit finite elements, *International Journal of Plasticity* 28 (1) (2012) 124 –
826 140.
- 827 [70] J. Simo, T. Hughes, *Computational inelasticity*, Springer-Verlag, New-York,
828 1998.
- 829 [71] A. M. Cuitiño, M. Ortiz, *Computational modelling of single crystals*, *Modelling*
830 *and Simulation in Materials Science and Engineering* 1 (3) (1993) 225 – 263.
- 831 [72] F. Barbe, L. Decker, D. Jeulin, G. Cailletaud, Intergranular and intragranular
832 behavior of polycrystalline aggregates. part 1: F.E. model, *International Journal*
833 *of Plasticity* 17 (4) (2001) 513 – 536.
- 834 [73] F. Barbe, S. Forest, G. Cailletaud, Intergranular and intragranular behavior of
835 polycrystalline aggregates. part 2: Results, *International Journal of Plasticity*
836 17 (4) (2001) 537 – 563.
- 837 [74] F. Barbe, R. Quey, A numerical modelling of 3d polycrystal-to-polycrystal dif-
838 fusive phase transformations involving crystal plasticity, *International Journal*
839 *of Plasticity* 27 (6) (2011) 823 – 840.

- 840 [75] S. Morito, H. Tanaka, R. Konishi, T. Furuhashi, T. Maki, The morphology and
841 crystallography of lath martensite in Fe-C alloys, *Acta Materialia* 51 (6) (2003)
842 1789 – 1799.
- 843 [76] S. Morito, X. Huang, T. Furuhashi, T. Maki, N. Hansen, The morphology and
844 crystallography of lath martensite in alloy steels, *Acta Materialia* 54 (19) (2006)
845 5323 – 5331.
- 846 [77] C. Farhat, F.-X. Roux, A method of finite element tearing and interconnecting
847 and its parallel solution algorithm, *International Journal for Numerical Methods*
848 *in Engineering* 32 (6) (1991) 1205 – 1227.
- 849 [78] C. Boher, O. Barrau, R. Gras, F. Rezai-Aria, A wear model based on cumulative
850 cyclic plastic straining, *Wear* 267 (5-8) (2009) 1087 – 1094.